

# INSIGHTS INTO THE FORMATION AND EVOLUTION HISTORY OF THE GALACTIC DISK SYSTEM

DOO RI HAN<sup>1</sup>, YOUNG SUN LEE<sup>2,4</sup>, YOUNG KWANG KIM<sup>2</sup>, AND TIMOTHY C. BEERS<sup>3</sup>

*Draft version, May 7, 2020*

## ABSTRACT

We present a kinematic analysis of a sample of 23,908 G- and K-type dwarfs in the Galactic disk. Based on the  $\alpha$ -abundance ratio,  $[\alpha/\text{Fe}]$ , we separated our sample into low- $\alpha$  thin-disk and high- $\alpha$  thick-disk stars. We find a  $V_\phi$  gradient of  $-28.2 \text{ km s}^{-1} \text{ dex}^{-1}$  over  $[\text{Fe}/\text{H}]$  for the thin disk, and an almost flat trend of the velocity dispersions of  $V_R$ ,  $V_\phi$ , and  $V_Z$  components with  $[\text{Fe}/\text{H}]$ . The metal-poor (MP;  $[\text{Fe}/\text{H}] < -0.3$ ) thin-disk stars with low- $V_\phi$  velocities have high eccentricities ( $e$ ) and small perigalacticon distances ( $r_p$ ), while the high- $V_\phi$  MP thin-disk stars possess low  $e$  and large  $r_p$ . Interestingly, half of the super metal-rich ( $[\text{Fe}/\text{H}] > +0.1$ ) stars in the thin disk exhibit low- $e$ , solar-like orbits. Accounting for the inhomogeneous metallicity distribution of the thin-disk stars with various kinematics requires radial migration by churning – it apparently strongly influences the current structure of the thin disk; we cannot rule out the importance of blurring for the high- $e$  stars. We derive a rotation velocity gradient of  $+36.9 \text{ km s}^{-1} \text{ dex}^{-1}$  for the thick disk, and decreasing trends of velocity dispersions with increasing  $[\text{Fe}/\text{H}]$ . The thick-disk population also has a broad distribution of eccentricity, and the number of high- $e$  stars increases with decreasing  $[\text{Fe}/\text{H}]$ . These kinematic behaviors could be the result of a violent mechanism, such as a gas-rich merger or the presence of giant turbulent clumps, early in the history of its formation. Dynamical heating by minor mergers and radial migration may also play roles in forming the current thick-disk structure.

*Keywords:* Methods: data analysis — technique: imaging spectroscopy — Galaxy: disk — stars: kinematics

## 1. INTRODUCTION

It has been almost four decades since the existence of the thick disk of the Milky Way (MW) was established by fitting double-exponential functions to the vertical density profile of stars in the Galactic disk (Yoshii 1982; Gilmore & Reid 1983). Tremendous progress in understanding the nature of the Galactic disk system has been made, in particular recently, thanks to the advent of large photometric and spectroscopic surveys such as the Sloan Digital Sky Survey (SDSS; York et al. 2000), the Radial Velocity Experiment (RAVE; Steinmetz et al. 2006), the Sloan Extension for Galactic Understanding and Exploration (SEGUE; Yanny et al. 2009), the *Gaia*-ESO survey (Gilmore et al. 2012), the Large sky Area Multi-Object Fiber Spectroscopic Telescope (LAMOST; Luo et al. 2015), the Apache Point Observatory Galactic Evolution Experiment (APOGEE; Majewski et al. 2017), and the GALactic Archaeology with HERMES (GALAH; De Silva et al. 2015).

The properties of the thick disk of the MW differ in many aspects from those of the thin disk. Briefly summarizing: (1) Spatially, the scale heights of the thin- and thick-disks are about 300 pc and 900 pc, respectively (Juric et al. 2008) (see also Bland-Hawthorn & Gerhard 2016 for a nice review on the scaleheight of each disk); (2) Kinematically, the orbital rotation velocity of the thick disk lags by about  $30 \text{ km s}^{-1}$  behind that of the thin

disk (Lee et al. 2011b; Jing et al. 2016), and the velocity dispersions of the thick disk are larger than those of the thin disk (Recio-Blanco et al. 2014; Guiglion et al. 2015; Wojno et al. 2016); (3) Chemically, the metallicity distribution function (MDF) of the thick-disk population peaks at between  $[\text{Fe}/\text{H}] = -0.5$  and  $-0.6$ , while that of the thin disk is at about  $[\text{Fe}/\text{H}] = -0.2$  (Wyse & Gilmore 1995; Soubiran et al. 2003; Kordopatis et al. 2011; Lee et al. 2011b). The  $\alpha$ -element abundance ratio with respect to Fe is higher by 0.2 to 0.3 dex for the thick disk than for the thin disk (Lee et al. 2011b; Adibekyan et al. 2013; Boeche et al. 2013; Anders et al. 2014; Hayden et al. 2015; Yan et al. 2019).

Note that, even though the disk system can be separated by the properties described above, an alternative interpretation has been advanced, that the thick disk is smoothly connected to the thin disk, rather than existing as an independent component (e.g., Bovy et al. 2012a,b). It has also been reported that the low-metallicity tail of the thick-disk MDF is an independent component, known as the metal-weak thick disk (MWTD). This component has lower metallicity (by at least a factor of two) and lower rotation velocity (by about  $30 \text{ km s}^{-1}$ ) than the canonical thick disk (Carollo et al. 2019). The independent nature of the MWTD has been further confirmed with large photometric survey data combined with accurate proper motions (An & Beers 2020). On the other hand, Adibekyan et al. (2011) reported, from an analysis of 1112 F, G, and K-type dwarfs, that in addition to the canonical thick-disk stars with enhanced  $[\alpha/\text{Fe}]$ , metal-rich thick-disk stars ( $[\text{Fe}/\text{H}] > -0.2$ ) with enhanced  $[\alpha/\text{Fe}]$  may exist as a separate component.

These observed differences between the two disk components strongly suggest that they have undergone dif-

<sup>1</sup> Department of Astronomy, Space Science, and Geology, Chungnam National University, Daejeon 34134, South Korea

<sup>2</sup> Department of Astronomy and Space Science, Chungnam National University, Daejeon 34134, South Korea

<sup>3</sup> Department of Physics and JINA Center for the Evolution of the Elements, University of Notre Dame, Notre Dame, IN 46556, USA

<sup>4</sup> Corresponding author: youngsun@cnu.ac.kr

ferent formation and evolutionary histories, as has been noted by many authors. [Abadi et al. \(2003\)](#), for example, used numerical simulations to propose that the MW has undergone a major merger at high redshift ( $z$ ), and a large fraction of stars have been accreted to form the thick disk from disrupted satellites during the merging process. According to this scenario, more than 60% of the thick-disk stars are comprised of debris of the tidally-disrupted satellite. [Villalobos & Helmi \(2008\)](#) reported from their MW-like simulations that a *minor* merger, for which the mass of the satellite accounts for only 10 – 20% of that of the host galaxy, led to the thick-disk formation. In this mechanism, the satellite galaxy serves to heat and tilt the disk of the host galaxy without destroying it, resulting in thickening a pre-existing thin disk.

Recently, [Helmi et al. \(2018\)](#) demonstrated that a 1:4 mass ratio merger, referred to as *Gaia*-Enceladus, could have produced the thick disk by dynamical heating of the pre-existing thin disk. The *Gaia*-Sausage may have affected the formation of the thick disk in a similar way ([Belokurov et al. 2018](#)). Studies by [Brook et al. \(2004, 2007, 2012\)](#) showed that the thick disk could also be formed from gas-rich building blocks, which were accreted during chaotic phase of hierarchical clustering at high redshift, while [Bournaud et al. \(2009\)](#) suggested that the thick disk formed from giant turbulent clumps, which undergo gravitational contraction and scatter stars at high  $z$ . All of these scenarios are associated with violent events for the formation of the thick disk.

In contrast to these violent scenarios, other studies have claimed that the formation of the thick disk could instead be the result of the cumulative effects of secular process associated with the radial migration of stars ([Sellwood & Binney 2002](#); [Schönrich & Binney 2009](#); [Loebman et al. 2011](#); [Roškar et al. 2012](#)). According to these authors, stars in the disk can effectively migrate radially inward or outward through the so-called *churning* and *blurring* processes. The *churning* process arises from the exchange of angular momentum stars with transient spiral structures; riding these spiral patterns, stars can migrate significant distances from their birth place within the disk. As stars move from the inner to the outer regions of the disk, they experience a weaker gravitational potential due to the decreasing mass density with increasing distance from the Galactic center, which results in larger vertically excursions from the plane. On the other hand, the *blurring* process is caused by the change of the epicycle amplitude of a star around its guiding center, without changing its angular momentum, through perturbations by giant molecular clouds. Some studies, however, have argued that the effect of radial migration may not be sufficient to significantly thicken the disk (e.g., [Minchev et al. 2012](#); [Kawata et al. 2017](#)).

As each formation model above predicts different (though perhaps not unique) characteristics of the resulting thick disk, there have been various efforts carried out to unravel the complex formation mechanism(s) through comparisons with the theoretical predictions. For example, [Sales et al. \(2009\)](#) noted distinct distributions of the stellar orbital eccentricities associated with various scenarios, and suggested that the use of the distribution of observed orbital eccentricities for the thick disk could help distinguish one from another. Although numerous

studies have employed a similar approach, using different stellar samples to explore the various formation mechanisms, they have thus far failed to pin down a unique model ([Wilson et al. 2011](#); [Dierickx et al. 2010](#); [Casetti-Dinescu et al. 2011](#); [Lee et al. 2011b](#); [Li & Zhao 2017](#); [Yan et al. 2019](#)).

In order to provide more stringent constraints on the suggested formation scenarios for the thick disk, one first needs to separate stars of the disk system into the thin- and thick-disk components, and investigate the detailed spatial, kinematic, and chemical properties of the stars belonging to each component. There have been several attempts to divide the disk stars into components by relying on their observed space motions (e.g., [Bensby et al. 2003, 2014](#); [Jing et al. 2016](#)). If a star is presently located in the same position as where it was born, and has the same kinematic properties as its natal molecular cloud, kinematic information could well be a powerful tool for this exercise. However, as it has become increasingly clear through investigations carried out with ever larger stellar samples, that is not likely to be the case. The birth places and kinematic properties of stars more likely change over time due to either major or minor mergers or secular evolution via perturbations by transient spiral patterns and giant molecular clouds.

By way of contrast, the chemistry of solar (and later-type) dwarf stars is essentially invariant during their main-sequence lifetimes. Thus, it provides a more stable and reliable indicator with which to classify disk-system stars into various components, provided that such components possess distinct chemical signatures. Among the various elemental-abundance ratios, the alpha-element-to-iron ratios ( $[\alpha/\text{Fe}]$ ) have proven useful for this exercise, as the  $[\alpha/\text{Fe}]$  ratios are larger by 0.2 – 0.3 dex for stars in the thick disk than for those in the thin disk (see [Bensby et al. 2003](#); [Reddy et al. 2006](#); [Fuhrmann 1998, 2008](#)). A number of studies ([Lee et al. 2011b](#); [Adibekyan et al. 2013](#); [Recio-Blanco et al. 2014](#); [Wojno et al. 2016](#); [Hayden et al. 2015, 2018](#); [Yan et al. 2019](#)) have been performed to investigate the kinematic properties of the stellar populations identified in the  $[\text{Fe}/\text{H}]$  versus  $[\alpha/\text{Fe}]$  plane, using the large amount of data from various spectroscopic surveys. Even though these studies were successful, to some degree, in reproducing hotter kinematic properties of the thick disk as well as the kinematic features of the thin disk, the formation mechanism of the thick disk has remained resistant to consensus.

This work is another effort to understand the formation mechanism of the thick disk. In this study, we utilize SEGUE G- and K-dwarfs in the Galactic disk, in order to explore their properties and compare with various thick-disk formation models. We make use of  $[\alpha/\text{Fe}]$  and  $[\text{Fe}/\text{H}]$  to chemically separate disk-system stars into the thin- and thick-disk populations, then examine the  $V_R$ ,  $V_\phi$ ,  $V_Z$  velocity components, their gradients with metallicity, their velocity dispersions, and the dynamical properties of each disk population. Based on our findings, we suggest likely formation and evolution histories of the Galactic disk system.

This paper is organized as follows. In Section 2, we describe the sample of G and K dwarfs, calculations of the velocity components and orbital parameters, and the method for the chemical separation of each disk population. We also discuss potential selection biases in our

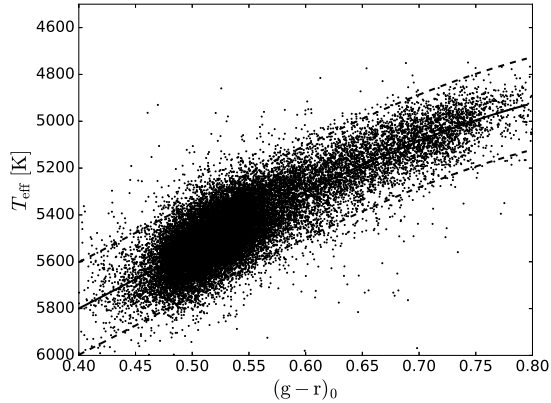


**Figure 1.** Distribution of candidate main-sequence dwarfs in the color-temperature plane. The black-solid curve is obtained from a least-square fit to the data; the dashed lines indicate  $\pm 2\sigma$  deviations from the fitted line. Stars located outside the dashed lines are removed from the sample in the remaining analysis.

sample. The results of the analyses of the kinematic and dynamical properties of each stellar population are presented in Section 3 and 4, respectively. We consider the plausible formation and evolution history of each disk in Section 5. Finally, we summarize our work in Section 6.

## 2. SEGUE G AND K DWARFS

### 2.1. Sample Selection

We first gathered stars that were specifically targeted as G and K dwarfs in SEGUE, in the dereddened color and magnitude ranges of  $0.45 < (g-r)_0 < 0.80$  and  $13.5 < r_0 < 20.5$ , respectively. From application of the SEGUE Stellar Parameter Pipeline (SSPP; Allende Prieto et al. 2008; Lee et al. 2008a,b, 2011a; Smolinski et al. 2011) on the medium-resolution ( $R \sim 2000$ ) spectra of those dwarfs, we determined the stellar atmospheric parameters ( $T_{\text{eff}}$ ,  $\log g$ , and  $[\text{Fe}/\text{H}]$ ) for each star. Typical errors of these estimated parameters from the SSPP are  $\sim 180$  K for  $T_{\text{eff}}$ ,  $\sim 0.24$  dex for  $\log g$ , and  $\sim 0.23$  dex for  $[\text{Fe}/\text{H}]$ . We also derived  $[\alpha/\text{Fe}]$  using the method of Lee et al. (2011a); the uncertainty of the estimated  $[\alpha/\text{Fe}]$  is typically better than 0.1 dex for signal-to-noise ratio (S/N) larger than 20. For reliable stellar parameters and  $[\alpha/\text{Fe}]$ , we applied this S/N cut to the entire sample.

Additionally, only stars with  $4500 < T_{\text{eff}} < 6000$  K and  $\log g > 3.8$  were included in our sample, in order to secure the most reliable identification of G and K dwarfs. As a final check, adopting a color-temperature relation for main-sequence stars, we removed stars more than  $2\sigma$  above or below the relation at a given  $(g-r)_0$ , as illustrated in Figure 1. The black-solid line in the figure comes from a least-square fit to the data, while the dashed lines are the  $\pm 2\sigma$  limits from this line. Even though this  $2\sigma$  limit is somewhat arbitrary, its purpose is to remove stars with erroneously determined  $T_{\text{eff}}$  (usually due to some defect in their spectra).

### 2.2. Calculations of Space Velocity Components and Orbital Parameters

In order to calculate the most precise velocity components for our program stars, we cross-matched our program stars with *Gaia* Data Release 2 (DR2) (Gaia Collaboration et al. 2018) in order to retrieve their proper

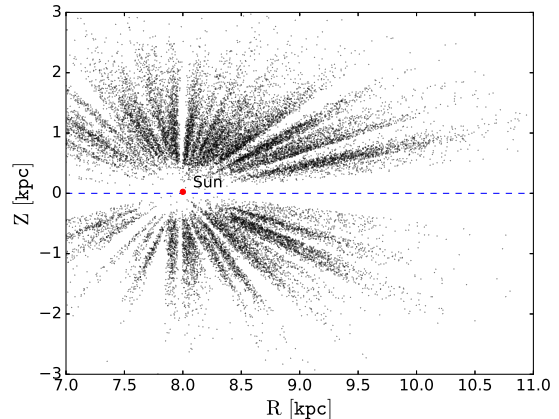


**Figure 2.** Spatial distribution of the final program sample in the  $R$  versus  $Z$  plane, which includes 23,908 SDSS/SEGUE G and K dwarfs. Note that the cuts applied as described in the text have already been applied here. The Sun (red dot) is located at  $(R, Z) = (8.0, 0.025)$  kpc; the blue dashed line at  $Z = 0$  kpc is the Galactic mid-plane.

motions and parallaxes. We selected stars with listed uncertainties in proper motion less than  $1.0 \text{ mas yr}^{-1}$ , and relative parallax errors smaller than 25% ( $=\sigma_\pi/\pi$ ), where  $\pi$  is the parallax and  $\sigma_\pi$  is the uncertainty. We also adjusted the parallaxes by the zero-point offset  $-0.029$  mas (Lindgren et al. 2018). We computed the distance by taking the inverse of the parallax for each star, and calculated the radial distance from the Galactic center projected onto the Galactic plane ( $R$ ), as well as the vertical distance from the Galactic plane ( $Z$ ). We assumed that the Sun is located at  $R = 8$  kpc and  $Z = 0.025$  kpc (Bland-Hawthorn & Gerhard 2016).

For a sanity check on the adoption of inverse-parallax distances from the *Gaia* catalog, we compared our derived distances with those estimated by a probabilistic inference approach (Bailer-Jones et al. 2018). We found from the sample of stars in common that the mean difference is  $-0.034$  kpc, with a standard deviation of 0.072 kpc. Although the mean offset becomes larger for more distant objects, the relative difference is less than 20% at 3 kpc, which is the typical uncertainty in estimating distances. Because our dwarf stars are predominantly located at a distance less than 3 kpc from the Sun, this offset suggests that the distance derived from taking the inverse of the *Gaia* parallaxes is suitable for our study. We note, however, that our derived distances may suffer from the Lutz-Kelker bias (Lutz & Kelker 1973), which causes an underestimate of our derived distance, especially for more distant objects, as they have larger relative errors ( $\sigma_\pi/\pi$ ).

Furthermore, by making use of the distances and proper motions, and adopting radial velocities from SEGUE spectra, we derived the space velocity components and orbital parameters, using the MWPotential2014 from galpy Python package<sup>5</sup> (Bovy 2015). This potential consists of a power-law density bulge and a Miyamoto-Nagai disk with mass  $6.8 \times 10^{10} M_\odot$ , and a Navarro-Frenk-White dark-matter halo profile.

We first derived  $U$ ,  $V$ ,  $W$  velocity components of mo-

<sup>5</sup> <http://jobovy.github.io/galpy>.

tion for each star, taking the peculiar motion of the Sun to be  $(U, V, W)_{\odot} = (-10.1, 4.0, 6.7) \pm (0.5, 0.8, 0.2) \text{ km s}^{-1}$  (Hogg et al. 2005), and the circular velocity of the local standard of rest (LSR) to be  $220 \text{ km s}^{-1}$  (Kerr & Lynden-Bell 1986). The positive direction of the  $U$  component is taken to be radially outward from the Galactic center. Solar orbital rotation is taken to be positive in the  $V$  direction, and  $W$  is positive in the direction of the North Galactic Pole. Additionally, the velocity components ( $V_R, V_{\phi}, V_Z$ ) in a cylindrical coordinate system were computed for each star. Among the orbital parameters, we derived the minimum distance ( $r_p$ ) and maximum distance ( $r_a$ ) from the Galactic center, and the maximum distance ( $Z_{\text{max}}$ ) from the Galactic plane reached during the orbit of a given star. The eccentricity ( $e$ ) is obtained from  $e = (r_a - r_p)/(r_a + r_p)$ .

In this paper, we are most interested in the stellar populations of the Galactic disk. As the typical halo star has low metallicity, slower orbital rotation velocity, and higher  $|W|$  velocity dispersion than its thick-disk counterparts, we further culled the sample by including only stars with  $[\text{Fe}/\text{H}] > -1.2$ ,  $|Z| < 3 \text{ kpc}$ , distance of  $d < 4 \text{ kpc}$ ,  $|W| < 100 \text{ km s}^{-1}$ , and rotation velocity of  $V_{\phi} > 50 \text{ km s}^{-1}$ , which will serve to minimize contamination from halo stars. We also restricted the sample to a range of  $7 < R < 11 \text{ kpc}$  along the disk plane, as our program stars predominantly reside in this region.

In summary, our final sample satisfies the following conditions:  $0.45 < (g-r)_0 < 0.80$  and  $13.5 < r_0 < 20.5$ ,  $4500 < T_{\text{eff}} < 6000 \text{ K}$ ,  $\log g > 3.8$ ,  $\text{S/N} > 20$ ,  $|Z| < 3 \text{ kpc}$ ,  $d < 4 \text{ kpc}$ ,  $7 < R < 11 \text{ kpc}$ ,  $[\text{Fe}/\text{H}] > -1.2$ ,  $V_{\phi} > 50 \text{ km s}^{-1}$ ,  $|W| < 100 \text{ km s}^{-1}$  for stars within  $2\sigma$  in the color-temperature relation of Figure 1. Figure 2 displays the spatial distribution of the final sample of 23,908 stars as black dots. The red dot at  $(R, Z) = (8.0, 0.025) \text{ kpc}$  is the Sun's location, and a blue-dashed line represents  $Z = 0 \text{ kpc}$ .

### 2.3. Chemical Separation of the Thin- and Thick-disk Populations

We chemically divide our program stars into the thin- and thick-disk populations based on their  $\alpha$ -abundance ratios (as a function of  $[\text{Fe}/\text{H}]$ , following the similar way by Lee et al. 2011b, as described below). Figure 3 shows histograms of the  $\alpha$ -abundance ratios over different cuts in  $[\text{Fe}/\text{H}]$ . With the exception of the lowest and highest metallicity bins, shown in the upper-left panel and lower-right panels, respectively, histograms for the remaining stars were split using steps of 0.1 dex, listed at the top of each panel. Then, assuming that each histogram consists of two unique stellar populations contributed by the thin disk and thick disk, we fitted Gaussians to each distribution. In this process, as the  $\alpha$ -distribution of the thick-disk component is rather broad in the range of  $-0.4 < [\text{Fe}/\text{H}] \leq -0.1$ , we first fitted a Gaussian to the thin-disk component to obtain its best-fit parameters; after fixing these, we derived the best-fit Gaussian for the thick-disk population. As there is no apparent contribution from the thin disk for the low-metallicity region ( $[\text{Fe}/\text{H}] < -0.7$ ) or from the thick disk for the highest metallicity region ( $[\text{Fe}/\text{H}] > +0.1$ ), we only fitted single Gaussian. The orange curves represent the best-fit lines for each component obtained from the Gaussian fits. Note that

we have explicitly not included any presumed contribution from the MWTD, which is shown as a distinct population from the canonical thick disk by recent studies (Carollo et al. 2019; An & Beers 2020).

We then identified boundary points (shown as the gray-solid lines in Figure 3) for the distributions in each metallicity bin. To accomplish this for the highest and two lowest metallicity cuts, where single Gaussian exists, we determined the  $[\alpha/\text{Fe}]$  value located  $3\sigma$  away from the mean. As a result, we obtained a first estimate of the division between the thin- and thick-disk populations. We repeated this exercise by shifting the metallicity range used in Figure 3 by  $+0.05 \text{ dex}$ , and obtained another set of boundary positions between the thin- and thick-disk populations. We then applied a linear least-square fit to the two sets of boundary points as a function of  $[\text{Fe}/\text{H}]$  to derive a dividing line of the two stellar populations. The resulting functional form is  $[\alpha/\text{Fe}] = -0.141 \times [\text{Fe}/\text{H}] + 0.140$  over the metallicity range of  $-0.65 < [\text{Fe}/\text{H}] < -0.25$ ; beyond this, we adopted constant values of  $[\alpha/\text{Fe}]$  to  $+0.232$  for  $[\text{Fe}/\text{H}] < -0.65$ , and  $+0.175$  for  $[\text{Fe}/\text{H}] > -0.25$ , respectively. Note that, for this exercise, we only considered stars with spectra having  $\text{S/N} > 50$  (hence the best  $[\alpha/\text{Fe}]$  and  $[\text{Fe}/\text{H}]$  determinations) in order to obtain the most reliable separation.

Our adopted chemical-dividing line between the two populations is shown as a solid-diagonal line in the left panel of Figure 4, which shows a logarithmic gray-scale plot of the number density of our dwarf sample in the  $[\text{Fe}/\text{H}]-[\alpha/\text{Fe}]$  plane. Each bin has a size of 0.025 by 0.01 dex in  $[\text{Fe}/\text{H}]$  and  $[\alpha/\text{Fe}]$ , respectively and has at least two stars. The figure clearly illustrates the two different populations as high- $\alpha$  (thick-disk) and low- $\alpha$  (thin-disk) sequences as a function of  $[\text{Fe}/\text{H}]$ ; the stars were assigned based on having distances from the solid line of more than  $\pm 0.05 \text{ dex}$  (shown as dashed lines), in order to accommodate the uncertainty in the derived  $[\alpha/\text{Fe}]$ . Stars in the region between the dashed lines and the solid lines are not assigned to either population. Through the application of this dividing scheme, we obtained 12,490 stars assigned to membership in the thin-disk population, and 6,712 stars assigned to the thick-disk population, and use these sub-samples below to carry out kinematic analysis.

### 2.4. Potential Selection Biases

Because the stars in our sample were selected for spectroscopic observations based on color and apparent magnitude, it may suffer from selection effects due to the target-selection algorithm used in SEGUE. For instance, in a magnitude-limited survey, because the metal-rich dwarfs are intrinsically brighter than the metal-poor dwarfs, there is a greater possibility to observe the metal-rich stars in a given field. On the other hand, the  $(g-r)_0$  color cut may preferentially include the lower-mass metal-poor stars relative to the slightly higher-mass metal-rich stars, as the former could outnumber the latter, resulting in biasing our sample towards including more low-metallicity stars. If there exists a significant metallicity bias in the SEGUE target selection, this may impact the dividing criterion we applied in Section 2.3, and our interpretations of the kinematic properties of the different components. Hence, we have carried out an exercise to test the sensitivity of our dividing scheme by

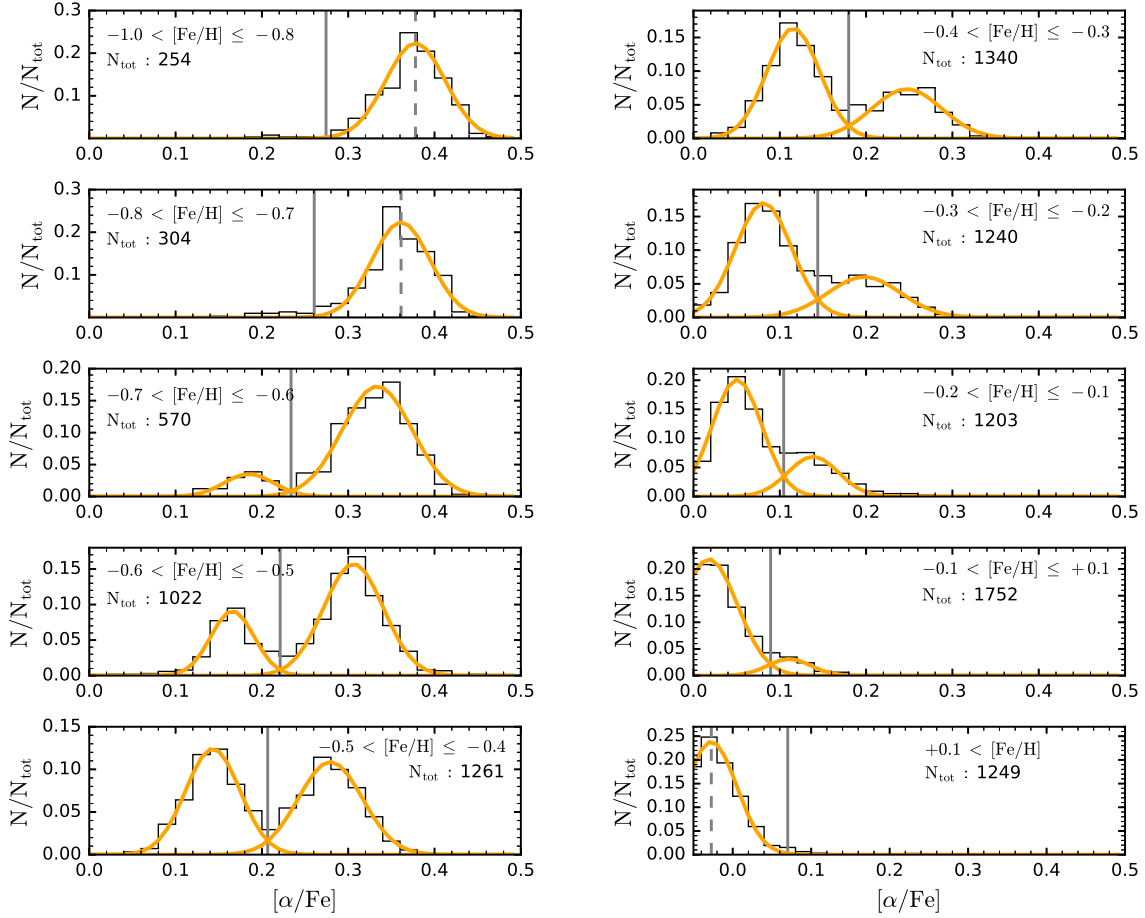


**Figure 3.** Histograms of  $[\alpha/\text{Fe}]$  for different  $[\text{Fe}/\text{H}]$  cuts. The black lines are the original data. The orange curves are derived from one or two Gaussian fits to each histogram. If two components exist, we use an iterative procedure to obtain division points (gray solid lines), as described in the text, between the two components. Gaussian models are then fit to the individual components. Note that in the range of  $-0.4 < [\text{Fe}/\text{H}] < -0.1$ , we first fit a Gaussian to the thin-disk component to find the best-fit parameters; after fixing these, we derived the best-fit Gaussian for the thick-disk population. For this procedure, we only consider stars with spectra having  $S/N > 50$ , in order to ensure a robust split.  $N_{\text{tot}}$ , listed in the legends, is the total number of stars in each panel.

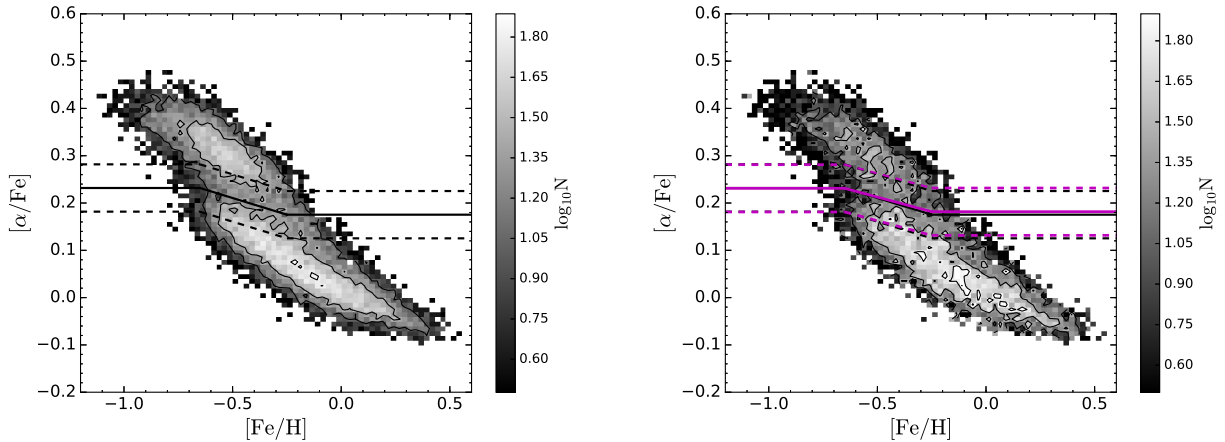


**Figure 4.** Left panel: Logarithmic gray-scale plot of the number density in the  $[\text{Fe}/\text{H}]$  versus  $[\alpha/\text{Fe}]$  plane, overlotted with equal density contours. Each bin has a size of 0.025 by 0.01 in  $[\text{Fe}/\text{H}]$  and  $[\alpha/\text{Fe}]$ , respectively, and contains at least two stars. The black-solid line is a reference point to aid in the separation of stars into the thin- and thick-disk components. The dashed lines are located at  $\pm 0.05$  dex in  $[\alpha/\text{Fe}]$  from the solid line (see text for further discussion). Right panel: Same as in the left panel, but for the selection bias-corrected distribution as described in the text. Note that we rescaled the number density by multiplying by the ratio of the total number of the original sample to that of the bias-corrected sample. The purple-solid line is the boundary between the thin- and thick-disk components, derived from the bias-corrected sample, while the black-solid line in this panel is the original (biased) sample. Note that their difference is negligible.

these potential biases.

First, we obtained the selection function for our G- and K-type dwarfs by adopting the similar methodology that other studies used (e.g., [Schlesinger et al. 2012](#); [Nandakumar et al. 2017](#); [Wojno et al. 2017](#); [Chen et al. 2018](#); [Mints & Hekker 2019](#)). The basic idea of the method is to derive the number ratio of the spectroscopically targeted objects to the photometrically available ones in a small bin on a color-magnitude diagram (CMD) for each SDSS plug-plate. In this process, we considered a bin size of 0.05 mag by 0.2 mag in color and magnitude, respectively, for a CMD of  $(g - r)_0$  and  $r_0$ . The selection function is regarded as the ratio of the number of stars selected for spectroscopic observation to the number of stars present in the direction of a given plug-plate with available photometry in each color and magnitude bin. After the calculations of the selection function, we corrected the selection bias of our dwarfs by multiplying the inverse of the selection function for each object.

Afterwards, we followed the exact same procedure described in Section 2.3 to derive the dividing line between the thin- and thick-disk populations. The right panel of Figure 4 shows the density map of the selection bias-corrected sample. The purple line denotes the boundary between the thin and thick disk, which was derived from the sample corrected for the selection bias, while the black-solid line from the original sample, which is not corrected for the selection bias. We notice the negligible difference between the two lines in the figure. Because we are not attempting to determine a precise metallicity distribution function from our sample, we decided to just use the original dwarf sample without the bias correction and the disk-separating criterion derived from the biased sample in the following analysis. This is also justified by the fact that because our sample was selected purely based on color and magnitude, it does not suffer from kinematic bias. Hence, any kinematic and dynamical properties that we are seeking to will not be greatly influenced by any potential selection bias caused by the color and magnitude.

### 3. KINEMATIC PROPERTIES OF THE THIN- AND THE THICK-DISK POPULATIONS

#### 3.1. Correlation of Rotation Velocity With Metallicity

Figure 5 shows the distributions of the  $V_R$ ,  $V_\phi$ , and  $V_Z$  velocity components, as a function of  $[\text{Fe}/\text{H}]$ , for the thin-disk (black dots) and thick-disk (red squares) populations. Each symbol represents a median value of 500 stars in a sample sorted in ascending order of  $[\text{Fe}/\text{H}]$ . The error bar is a standard deviation obtained from bootstrapping of the sample 1000 times. The two solid lines representing the velocity gradients are obtained by a least-square fit to the median values of each population. The derived slope of each velocity component for each population is indicated in the legend of each panel. We also performed a least-square fit to the entire sample for each velocity component, and found no discernible discrepancy within the derived uncertainties of the gradients, compared to those in Figure 5.

From inspection of Figure 5, there exist only small gradients for  $V_R$  and  $V_Z$  velocities with metallicity for both populations, as found in previous studies (e.g., [Guiglion et al. 2015](#); [Wojno et al. 2016](#)), even though the  $V_Z$  gradient for the thick disk has a relatively larger uncertainty.

**Table 1**  
Summary of Kinematics for Thin- and Thick-Disk Populations

Gradients with Metallicity ( $\text{km s}^{-1} \text{dex}^{-1}$ )		
Component	Thin disk	Thick disk
$\partial V_R / \partial [\text{Fe}/\text{H}]$	$-4.8 \pm 2.4$	$2.5 \pm 2.6$
$\partial V_\phi / \partial [\text{Fe}/\text{H}]$	$-28.2 \pm 1.5$	$36.9 \pm 3.3$
$\partial V_Z / \partial [\text{Fe}/\text{H}]$	$-3.3 \pm 1.1$	$2.4 \pm 4.7$
$\partial \sigma_{V_R} / \partial [\text{Fe}/\text{H}]$	$0.6 \pm 1.2$	$-43.2 \pm 4.6$
$\partial \sigma_{V_\phi} / \partial [\text{Fe}/\text{H}]$	$1.9 \pm 0.6$	$-17.4 \pm 2.6$
$\partial \sigma_{V_Z} / \partial [\text{Fe}/\text{H}]$	$-6.0 \pm 1.2$	$-20.6 \pm 1.4$
Mean Velocities and Velocity Dispersions ( $\text{km s}^{-1}$ )		
Component	Thin disk	Thick disk
$\langle V_R \rangle$	$0.1 \pm 0.4$	$3.8 \pm 0.8$
$\langle V_\phi \rangle$	$197.2 \pm 0.2$	$159.2 \pm 0.5$
$\langle V_Z \rangle$	$0.9 \pm 0.2$	$0.6 \pm 0.5$
$\langle \sigma_{V_R} \rangle$	$40.2 \pm 0.3$	$62.9 \pm 0.5$
$\langle \sigma_{V_\phi} \rangle$	$26.0 \pm 0.2$	$39.1 \pm 0.3$
$\langle \sigma_{V_Z} \rangle$	$21.3 \pm 0.2$	$38.1 \pm 0.3$

**Note.** — The errors in the mean and dispersion are based on 1000 bootstrap re-samples. The mean of the velocity and dispersion is calculated by taking an average of the symbols for each population in Figures 5 and 6, respectively.

By contrast, the  $V_\phi$  gradients for the thick and thin disks are highly significant, and of opposite signs:  $+36.9 \pm 3.3 \text{ km s}^{-1} \text{ dex}^{-1}$  and  $-28.2 \pm 1.5 \text{ km s}^{-1} \text{ dex}^{-1}$ , respectively. Moreover, the mean of the  $V_\phi$  component of the thin disk ( $+197.2 \pm 0.2 \text{ km s}^{-1}$ ) is significantly larger than that of the thick disk ( $+159.2 \pm 0.5 \text{ km s}^{-1}$ ), a collective lag in the rotational velocity of the thick disk that has been reported by numerous previous authors (e.g., [Guiglion et al. 2015](#); [Rojas-Arriagada et al. 2016](#); [Belokurov et al. 2020](#)).

We recall results on  $V_\phi$  gradients with  $[\text{Fe}/\text{H}]$  reported by a number of previous studies. From a sample of SEGUE G dwarfs with less-precise distances and proper motions, [Lee et al. \(2011b\)](#) reported a  $V_\phi$  gradient of  $+45.8 \pm 2.9 \text{ km s}^{-1} \text{ dex}^{-1}$  and  $-22.3 \pm 1.6 \text{ km s}^{-1} \text{ dex}^{-1}$  and for the thick and thin disk, respectively. [Adibekyan et al. \(2013\)](#) examined F-, G-, and K-type dwarfs from the HARPS sample ([Mayor et al. 2003](#); [Lo Curto et al. 2010](#); [Santos et al. 2011](#)), and derived  $V_\phi$  gradients of  $+41.9 \pm 18.1 \text{ km s}^{-1} \text{ dex}^{-1}$  and  $-16.8 \pm 3.7 \text{ km s}^{-1} \text{ dex}^{-1}$  for the thick disk and thin disk, respectively. [Recio-Blanco et al. \(2014\)](#), using *Gaia* ESO F-, G-, and K-type stars, reported values for the  $V_\phi$  slopes of  $+43 \pm 13 \text{ km s}^{-1} \text{ dex}^{-1}$  and  $-17.6 \pm 6 \text{ km s}^{-1} \text{ dex}^{-1}$  for the thick and thin disk, respectively. The studies by [Guiglion et al. \(2015\)](#) and [Wojno et al. \(2016\)](#) reported a  $V_\phi$  gradient of  $+49 \pm 10 \text{ km s}^{-1} \text{ dex}^{-1}$  and  $+51 \pm 10 \text{ km s}^{-1} \text{ dex}^{-1}$ , respectively, for the thick-disk population, which agree with our values within the errors. As for the thin disk, [Wojno et al. \(2016\)](#) found  $-11 \pm 1 \text{ km s}^{-1} \text{ dex}^{-1}$ , whereas [Guiglion et al. \(2015\)](#) claimed a positive rotation velocity gradient. They argued that this is because their sample covers a larger metallicity range ( $-1.0 < [\text{Fe}/\text{H}] < +0.5$ ) than other studies. They indeed found a slightly negative gradient of  $-5 \pm 5 \text{ km s}^{-1} \text{ dex}^{-1}$  by narrowing the metallicity range ( $-0.7 < [\text{Fe}/\text{H}] < +0.2$ ), but still less steep than others. From

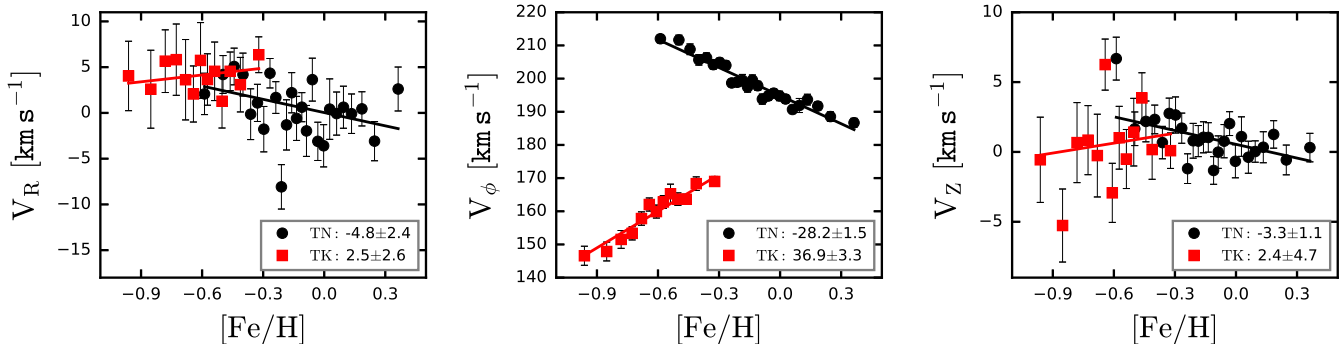


**Figure 5.** Trend of median values of  $V_R$  (left),  $V_\phi$  (middle), and  $V_Z$  (right) velocity components over metallicity. The black dots are for the thin-disk stars, and the red squares for the thick-disk stars. Each symbol represents a median value of 500 stars and error bars are calculated by bootstrapping of the sample in each symbol 1000 times. The two-solid lines, which show the velocity gradients are obtained by the least square fit to the median values. The slope of each velocity component for each population is denoted with its associated uncertainty in the square box.

giants observed by LAMOST with *Gaia* DR2 astrometry, Yan et al. (2019) found a positive slope ( $+30.87 \pm 0.001 \text{ km s}^{-1} \text{ dex}^{-1}$ ) and negative slope ( $-17.03 \pm 0.001 \text{ km s}^{-1} \text{ dex}^{-1}$ ) for the thick and thin disk, respectively. Interestingly, their slope of the gradient in the thick disk is much shallower than found by other studies.

Re Fiorentin et al. (2019) carried out a thorough investigation of the rotation velocity gradient with metallicity at various distances from the Galactic center, using 58,882 red giants from APOGEE DR14 (Abolfathi et al. 2018) and proper motions from *Gaia* DR2. For the thick-disk population, they derived slopes between  $+20.7$  and  $+60.1 \text{ km s}^{-1} \text{ dex}^{-1}$ , increasing with distance from the Galactic center. At the Solar radius ( $R \sim 8 \text{ kpc}$ ), their reported gradient was  $+43.5 \text{ km s}^{-1} \text{ dex}^{-1}$ . They consistently found negative gradients for the thin-disk population over  $5 < R < 13 \text{ kpc}$ , in the range  $-43.8$  to  $-16.3 \text{ km s}^{-1} \text{ dex}^{-1}$ , the lowest at the Solar radius.

We have carried out a similar exercise. After dividing our sample into three regions:  $7 < R \leq 8 \text{ kpc}$ ,  $8 < R \leq 9 \text{ kpc}$ , and  $9 < R \leq 11 \text{ kpc}$ , we derived gradients of  $-34.0 \pm 2.4 \text{ km s}^{-1} \text{ dex}^{-1}$ ,  $-27.6 \pm 1.2 \text{ km s}^{-1} \text{ dex}^{-1}$ , and  $-28.4 \pm 1.8 \text{ km s}^{-1} \text{ dex}^{-1}$ , respectively, for the thin disk, and  $27.7 \pm 4.0 \text{ km s}^{-1} \text{ dex}^{-1}$ ,  $42.1 \pm 3.5 \text{ km s}^{-1} \text{ dex}^{-1}$ , and  $61.2 \pm 7.6 \text{ km s}^{-1} \text{ dex}^{-1}$ , respectively, for the thick disk. Even though the magnitudes of the gradients are slightly different, the overall trends with Galactocentric distance are the same as found by Re Fiorentin et al. (2019).

To summarize, our derived  $V_\phi$  gradient ( $+36.9 \text{ km s}^{-1} \text{ dex}^{-1}$ ) for the thick disk generally agrees with those from other studies mentioned above. However, it appears that our  $V_\phi$  gradient ( $-28.2 \text{ km s}^{-1} \text{ dex}^{-1}$ ) of the thin disk is slightly steeper, by about  $-10 \text{ km s}^{-1} \text{ dex}^{-1}$ , than other studies. The main source of the difference is the spatial coverage of the thin-disk stars considered. While our chemically separated thin-disk stars include many objects (about 41%) in the region  $|Z| > 0.8 \text{ kpc}$ , the thin-disk samples in the aforementioned studies consist of stars predominantly in the region  $|Z| < 0.8 \text{ kpc}$ . Indeed, when we restrict our thin-disk stars to the region  $|Z| < 0.8 \text{ kpc}$ , we obtain a less-steep gradient, of about  $-25 \text{ km s}^{-1} \text{ dex}^{-1}$ . The reason our sample includes many thin-disk stars with  $|Z| > 0.8 \text{ kpc}$  is likely due to the combination of the sampling region in the SEGUE survey and its target-selection strategy. The bright limit of

**Table 2**  
Kinematic Parameters used for Membership Probability

Parameter	Thin	Thick
X	0.94	0.06
$\sigma_U$ ( $\text{km s}^{-1}$ )	43	67
$\sigma_V$ ( $\text{km s}^{-1}$ )	28	51
$\sigma_W$ ( $\text{km s}^{-1}$ )	17	42
$V_{\text{asy}}$ ( $\text{km s}^{-1}$ )	-9	-48

**Note.** — X represents the fraction of thin- or thick-disk stars, and  $V_{\text{asy}}$  is the asymmetric drift relative to the LSR.

the SDSS photometry hinders the observation of (bright) stars close to the Galactic plane.

### 3.2. Velocity Dispersion Gradients with Metallicity

Figure 6 exhibits the trends of  $V_R$ ,  $V_\phi$ , and  $V_Z$  velocity dispersions with metallicity. Following the same procedure as in Figure 5, we derived the slope of the velocity dispersion for each velocity component; the same symbols are used as in Figure 5. The figure clearly shows that the chemically selected thick-disk population exhibits higher velocity dispersions and steeper gradients than the thin-disk population for all velocity components. Table 1 summarizes the gradient of each velocity component and velocity dispersion, and their mean values, calculated by averaging the median points for each population in Figures 5 and 6. From inspection of the table, the  $V_R$  component exhibits the largest velocity dispersion and the steepest dispersion gradient among the three velocity components of the thick disk.

One notable feature in Figure 6 is that, unlike the velocity gradient, a negative slope is found for  $\sigma_{V_R}$ ,  $\sigma_{V_\phi}$ , and  $\sigma_{V_Z}$  for the thick-disk population, as a function of metallicity, whereas the thin-disk stars exhibit an almost flat velocity dispersion gradient for all three velocity components. However, a clear increase of  $\sigma_{V_Z}$  with decreasing metallicity is seen for the more metal-poor ( $[\text{Fe}/\text{H}] < -0.3$ ) thin-disk stars in the metal-poor region (right panel of Figure 6). The dispersion at  $[\text{Fe}/\text{H}] = -0.6$  is as high as that of the thick disk at  $[\text{Fe}/\text{H}] = -0.3$ .

Due to the results above, we investigated the hotter kinematics of the metal-poor thin-disk stars (MPTN;  $[\text{Fe}/\text{H}] < -0.3$ ) if these could arise because of contamination from thick-disk stars, following the method de-

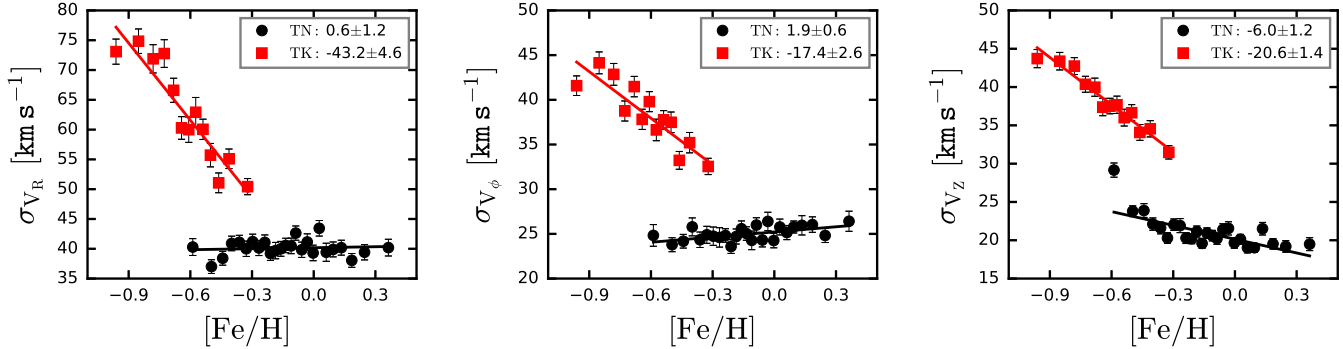


**Figure 6.** Same as in Figure 5, but for  $V_R$ ,  $V_\phi$ , and  $V_z$  velocity dispersions.

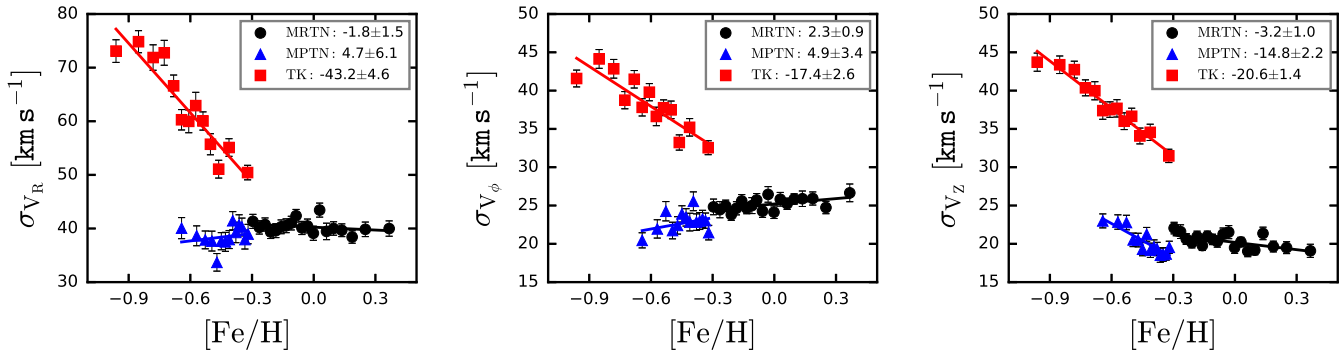


**Figure 7.** Same as in Figure 5, but the thin-disk population is divided into metal-rich (black dots;  $[\text{Fe}/\text{H}] > -0.3$ ) and metal-poor (blue triangles;  $[\text{Fe}/\text{H}] \leq -0.3$ ) groups, indicated in the legends as MRTN and MPTN, respectively. The metal-poor group only includes stars with thin-disk kinematics (see text for more details). The blue triangles are the median value of 200 stars, while the black dots are a median value for 500 stars.

**Table 3**  
Mean Values of Velocities, Velocity Dispersions, and  $[\alpha/\text{Fe}]$  for MRTN and MPTN Stars

	$N$	$\langle V_R \rangle$ ( $\text{km s}^{-1}$ )	$\langle V_\phi \rangle$ ( $\text{km s}^{-1}$ )	$\langle V_z \rangle$ ( $\text{km s}^{-1}$ )	$\langle \sigma_{V_R} \rangle$ ( $\text{km s}^{-1}$ )	$\langle \sigma_{V_\phi} \rangle$ ( $\text{km s}^{-1}$ )	$\langle \sigma_{V_z} \rangle$ ( $\text{km s}^{-1}$ )	$\langle [\alpha/\text{Fe}] \rangle$
MRTN	9466	-0.7	194.1	0.6	40.4	25.6	20.4	0.03
MPTN	2855	2.9	208.2	2.2	38.7	23.1	20.4	0.11

**Note.** —  $N$  is the number of stars. Possible contaminating thick-disk stars have been excluded (see text for details).

scribed by [Bensby et al. \(2003, 2014\)](#). The basic idea is that, by assuming that stars of the thin- and thick-disk populations have Gaussian distributions with different space velocities ( $U$ ,  $V$ , and  $W$ ) and asymmetric drift, stars can be separated by their probability of belonging to one or the other population. We employed the parameters listed in Table 2, which are adopted from [Reddy et al. \(2006\)](#). In the table,  $X$  is the fraction of stars that belong to each disk component in the local sample of stars. If a star has a higher likelihood of being a member of the thick disk, relative to the thin disk, that is,  $\text{Pr}(\text{TK})/\text{Pr}(\text{TN}) > 0.5$ , this star is assigned to the thick disk. On the other hand, thin-disk membership is assigned if a star has  $\text{Pr}(\text{TK})/\text{Pr}(\text{TN}) < 0.5$ . We applied this procedure to the MPTN stars, and found that among the 3,024 chemically separated MPTN stars, 2,855 stars are kinematically assigned to the thin disk, while the number of the stars assigned to the thick disk is only 169, suggesting that contamination from the thick-disk

stars in the thin-disk subsample is minimal.

From the kinematically identified metal-poor thin-disk stars with  $[\text{Fe}/\text{H}] < -0.3$ , we have examined the distribution of the velocity dispersions again, as shown in Figure 7. The MPTN stars are represented with blue triangles; each triangle corresponds to 200 stars. We can see that the  $V_z$  velocity dispersion of the MPTN stars increases with decreasing metallicity, and its trend is similar to that of the MPTN stars in Figure 6, whereas the  $V_R$  and  $V_\phi$  velocity dispersions exhibit almost no gradients. By comparison, the  $V_R$  and  $V_z$  dispersion gradients of the metal-rich thin-disk (MRTN;  $[\text{Fe}/\text{H}] > -0.3$ ) stars are almost flat, while the slope of the  $V_\phi$  component exhibits a small positive value. These stars are represented by black dots in Figure 7; each black dot corresponds to 500 stars.

Table 3 lists the total numbers and mean values of the velocity components, their velocity dispersions, and  $[\alpha/\text{Fe}]$  for the MRTN and MPTN stars. Note that the



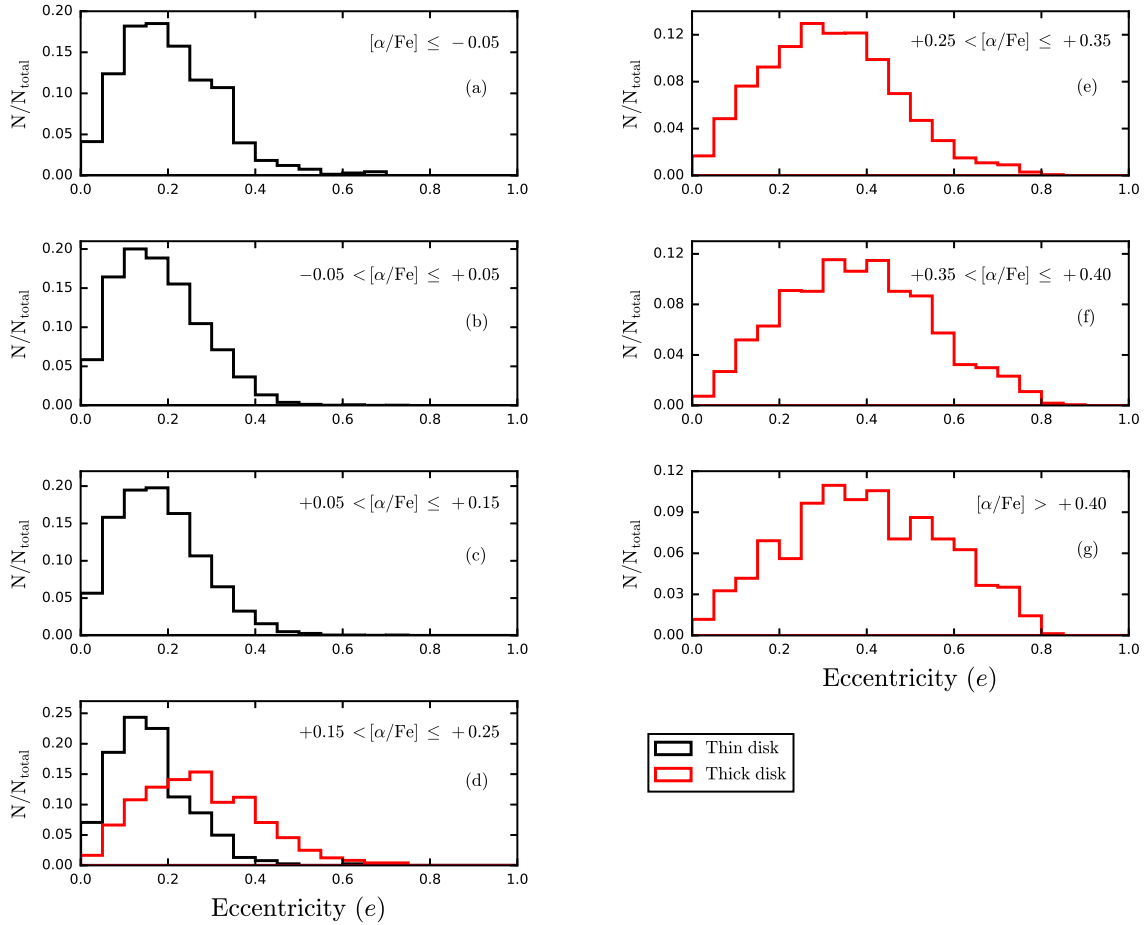


**Figure 8.** Histograms of eccentricities for the thin-disk (black line) and the thick-disk (red line) stars in different  $[\alpha/\text{Fe}]$  bins, as indicated in the legends of each panel. The  $[\alpha/\text{Fe}]$  range increases from (a) to (g).

MPTN stars do not include the objects with probable thick-disk kinematics rejected as above. The dispersions of the  $V_R$  and  $V_Z$  components of the MPTN stars are nearly the same as the ones from the entire thin-disk stars (see Table 1), but  $\sigma_{V_\phi}$  is slightly smaller. We also observe that  $\langle V_\phi \rangle$  becomes a little bit larger, while the change in  $\langle V_R \rangle$  and  $\langle V_Z \rangle$  is very small. We conclude from these results that the small possible contamination from stars with thick-disk kinematics in the MPTN subsample has little effect on our results. Thus, our chemical criterion for thin- and thick-disk separation appears quite robust, and suitable for investigations of the kinematics of each population. In this regard, it is worth mentioning that Rojas-Arriagada et al. (2016) distinguished thin-disk stars into three groups: metal-rich, metal-intermediate (MI), and metal-poor (MP) stars. The MI and MP regions are divided at  $[\text{Fe}/\text{H}] \sim -0.25$ , which is close to our adopted dividing value. They investigated the dispersion of rotation velocity for each population, and identified a higher dispersion for the MPTN stars than for the MITN and MRTN populations. Furthermore, a close examination of the right panel of Figure 7 clearly indicates some offset in  $\sigma_{V_Z}$  between the MRTN and MPTN samples. This may support the claim of an independent evolution of MPTN stars by Rojas-Arriagada et al. (2016).

Comparing with other studies, Wojno et al. (2016)

found velocity dispersions of  $(\sigma_{V_R}, \sigma_{V_\phi}, \sigma_{V_Z}) = (32, 19, 15)$  km s $^{-1}$  in cylindrical coordinates for the thin disk, and  $(\sigma_{V_R}, \sigma_{V_\phi}, \sigma_{V_Z}) = (49, 36, 29)$  km s $^{-1}$  for the thick disk. These values are slightly lower than ours, as listed in Table 1. Interestingly, Recio-Blanco et al. (2014) reported no significant slope in  $\sigma_{V_\phi}$  and  $\sigma_{V_Z}$  for the two disk populations, and found similar rotation velocity dispersions (about 45 km s $^{-1}$ ) for both the thin disk and thick disks at  $[\text{Fe}/\text{H}] \sim -0.3$ . Li & Zhao (2017) derived a vertical velocity dispersion ( $\sigma_{V_Z}$ ) of  $58.8 \pm 0.3$  km s $^{-1}$  dex $^{-1}$  for the thick disk from 2035 giants observed by LAMOST, a value much larger than reported by the other studies (including ours). Hayden et al. (2020) investigated about 62,000 stars from GALAH, and calculated a vertical velocity dispersion of about 8 km s $^{-1}$  at  $[\alpha/\text{Fe}] = 0$  and  $[\text{Fe}/\text{H}] = 0$ , increasing to over 50 km s $^{-1}$  for more  $\alpha$ -enhanced, metal-poor stars. Belokurov et al. (2020) obtained  $(\sigma_{V_R}, \sigma_{V_\phi}, \sigma_{V_Z}) = (31 \pm 6, 21 \pm 4, 26 \pm 5)$  km s $^{-1}$  and  $(\sigma_{V_R}, \sigma_{V_\phi}, \sigma_{V_Z}) = (73 \pm 7, 47 \pm 6, 48 \pm 6)$  km s $^{-1}$  for the thin- and thick-disk stars, respectively, in the ranges of  $2 < |Z| < 3$  kpc and  $-0.7 < [\text{Fe}/\text{H}] < -0.2$ . The dispersions of their thin-disk population generally agree well with ours, taking into account the quoted uncertainties, but those of their thick-disk population are slightly higher than ours.

Summarizing, the different trends of the velocities

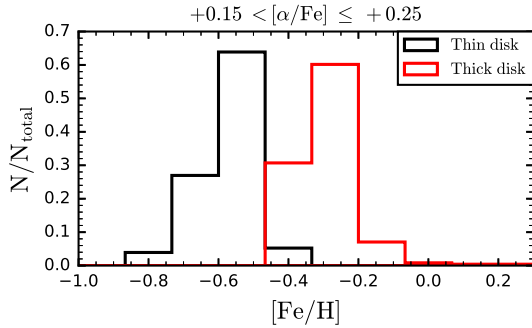


**Figure 9.** Metallicity distribution functions (MDFs) of the thin-disk (black line) and thick-disk (red line) stars in the range of  $+0.15 < [\alpha/\text{Fe}] \leq +0.25$ .

and velocity dispersions over  $[\text{Fe}/\text{H}]$  between the thin- and thick-disk populations reported here and elsewhere clearly imply that the two populations had different star-formation and/or evolutionary histories. In particular, the negative slope of the rotation velocity for the thin disk may indicate that the radial mixing plays an important role in shaping its current form.

#### 4. DYNAMICAL PROPERTIES OF THE THIN AND THICK DISKS

##### 4.1. Eccentricity Distribution Over $[\alpha/\text{Fe}]$

Among the available stellar dynamical properties, the eccentricity distribution of a given population is a very useful tracer of its origin and evolution. For example, Sales et al. (2009) investigated the distribution of the eccentricities of thick-disk stars simulated from four different thick-disk formation scenarios, and reported that the orbital eccentricity distribution of each model exhibits distinctly different properties. Thus, in order to characterize the likely formation history of our chemically separated thick-disk population, we have considered the eccentricities of the stars over different ranges of  $[\alpha/\text{Fe}]$ , as shown in Figure 8. In this figure, the range of  $[\alpha/\text{Fe}]$  is indicated in the legend at the top right of each panel, and increases from the top-left to the bottom-right panel (e.g., from (a) to (g)).

Inspection of Figure 8 reveals that the thin-disk population (black line in the figure) has a skewed distribution up to relatively high eccentricity,  $e \sim 0.5$ , with a peak at a value  $e < 0.2$ . It is also interesting to note that the width of the distribution becomes narrower as one moves toward higher values of  $[\alpha/\text{Fe}]$ . In other words, the fractions of high  $e$ -stars decrease with increasing  $[\alpha/\text{Fe}]$ . On the other hand, the thick disk (red line) exhibits a much broader distribution of orbital eccentricities, with an extended tail to much higher  $e$ . The  $e$ -distribution of the thick disk becomes broader with increasing  $[\alpha/\text{Fe}]$ , and there are greater fractions of high- $e$  stars, resulting in a shift of the peak to higher  $e$ . Close inspection at the overlapping region at  $+0.15 < [\alpha/\text{Fe}] < +0.25$  indicates that the distributions of the two populations appear very different. The peak of the eccentricity distribution of the thick disk clearly occurs at higher  $e$  than that of the thin disk in this range of  $[\alpha/\text{Fe}]$ .

In order to examine the region of  $+0.15 < [\alpha/\text{Fe}] < +0.25$  more closely, we have considered the MDFs of the thin- and thick-disk populations (see Figure 9). The

black histogram is for the thin disk, while the red histogram is for the thick disk. The two populations clearly exhibit very different MDFs. The MDF of the metal-poor thin-disk population peaks at  $[\text{Fe}/\text{H}] = -0.55$ , compared to  $[\text{Fe}/\text{H}] = -0.25$  for the metal-rich thick-disk population. The width of each distribution is almost the same, however. This suggests that they have experienced different chemical-evolution histories, even though they share similar  $\alpha$ -abundance ratios.

The general properties of our derived eccentricity distributions for the two disks qualitatively agree with previous studies. For instance, Hayden et al. (2018) studied the Galactic disk with 3,000 stars from the *Gaia*-ESO survey, and reported not only the increasing trend of eccentricity with increasing  $[\text{Mg}/\text{Fe}]$ , but also a median eccentricity of  $e \sim 0.33$  for the high- $[\text{Mg}/\text{Fe}]$ , metal-poor stars, which is very similar to our value (0.4) of the peak eccentricity for  $[\alpha/\text{Fe}] > +0.40$ . Using giants observed by LAMOST with available *Gaia* DR2 astrometry, Yan et al. (2019) found an increasing trend of orbital eccentricities with decreasing metallicity for the thick-disk population. We can infer this trend in Figure 8 as well, because  $[\alpha/\text{Fe}]$  generally increases with decreasing  $[\text{Fe}/\text{H}]$ , as can be seen in Figure 4.

According to the study by Sales et al. (2009), the eccentricity distribution of thick-disk stars formed through heating by minor mergers exhibits a secondary peak. However, since our results in Figure 8 do not appear to have a secondary peak for all  $[\alpha/\text{Fe}]$  bins, we can rule out this scenario. Note, however, that the existence of the high eccentricity secondary peak may depend on the initial conditions of the interacting dwarf galaxies in the simulation. On the other hand, the eccentricity distribution of the accretion model seems similar to that of panel (g) of Figure 8, even though the peak of panel (g) is lower than the prediction of the model. Nevertheless, it cannot explain the change in the distribution with  $[\alpha/\text{Fe}]$ , and the lack of stars with significantly high eccentricity stars in this panel. Consequently, we can discard this scenario as a mechanism for the thick-disk formation as well. Considering the migration and merger models, it is hard to tell quantitatively from the eccentricity distribution which one is a better prescription for thick-disk formation, as they predict qualitatively very similar  $e$ -distribution to our results. To distinguish one from the other, we consider the investigation described below.

##### 4.2. Distribution of Eccentricities and Perigalactic Distances in the $R$ - $V_\phi$ Plane

In this section, we examine the orbital properties of the MPTN ( $[\text{Fe}/\text{H}] < -0.3$ ), super metal-rich ( $[\text{Fe}/\text{H}] > +0.1$ ) thin-disk (SMRTN), and the thick-disk populations in greater detail. Figure 10 compares how the eccentricity (left panels) and perigalactic distance distributions (right panels) differ, in the  $R$ - $V_\phi$  plane, between the MP (upper panels) and SMR (lower panels) populations of the thin disk. In the upper-left panel of Figure 10, for the MPTN stars, we observe a group of stars (hereafter, G1) with high eccentricity ( $e > 0.2$ ) and low orbital rotation velocity ( $V_\phi < 170 \text{ km s}^{-1}$ ). Stars with similar properties to G1 can also be seen in the bottom-left panel for the SMR stars. One clear difference for stars with  $e > 0.2$  between the MP and SMR stars is that almost all of the SMRTN stars have  $V_\phi < 180 \text{ km s}^{-1}$ , while there are also

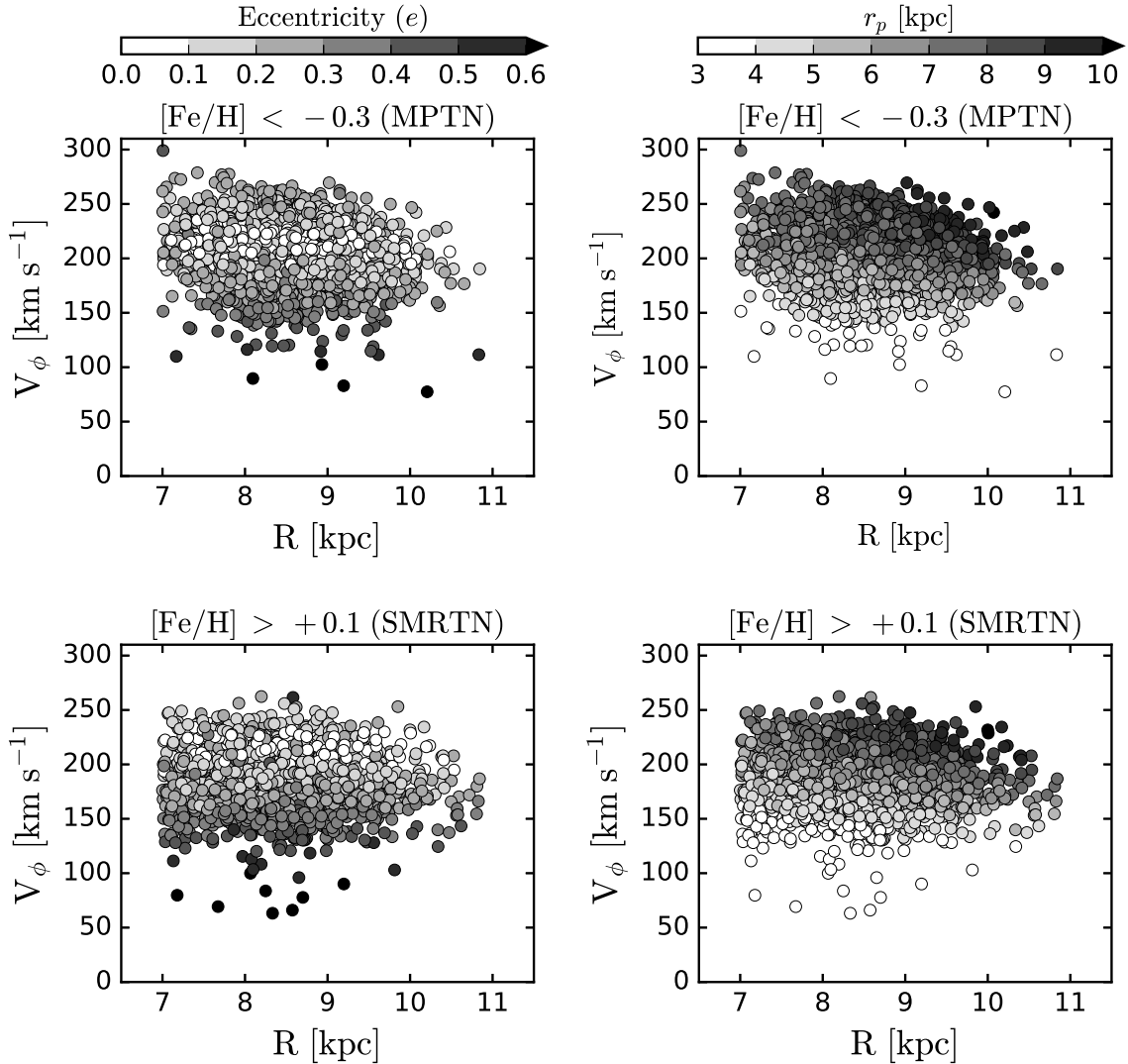


**Figure 10.** Left panels: Gray-scale distribution of eccentricities of metal-poor (upper panel;  $[\text{Fe}/\text{H}] < -0.3$ ) and super metal-rich (bottom panel;  $[\text{Fe}/\text{H}] > +0.1$ ) thin-disk stars in the  $R$ - $V_\phi$  plane.  $R$  is the Galactocentric distance projected onto the Galactic plane. The gray-scale bar represents the scale of the eccentricity. Right panels: Same as in the left panels, but for the perigalactic distance ( $r_p$ ).

high- $V_\phi$  stars ( $> 240 \text{ km s}^{-1}$ ) in the MPTN population. The stars with  $e < 0.1$  are mostly concentrated between  $V_\phi = 190$  and  $220 \text{ km s}^{-1}$  in both populations.

The upper-right panel of Figure 10 indicates, as expected, that the  $r_p$  distance correlates with  $R$ , such that as the Galactocentric distance increases, the perigalactic distance increases as well. In addition, there is a tendency for the  $V_\phi$  velocity to increase as the  $r_p$  distance increases at a given  $R$ . It also appears that the MPTN stars show a negative correlation between  $V_\phi$  and  $R$ , whereas no such trend exists for the SMRTN stars (see the right panels of Figure 10).

Quantitatively, we estimated that approximately 52% of the stars with  $V_\phi > 240 \text{ km s}^{-1}$  are on circular orbits ( $e \leq 0.2$ ) for the MPTN population. These high- $V_\phi$  stars have a median value of  $r_p \sim 8.3 \text{ kpc}$  and  $r_a \sim 11.5 \text{ kpc}$ , suggesting that most of them move around the Galactic center in the outer edge of the Solar circle. Mikolaitis et al. (2014) and Rojas-Arriagada et al. (2016) also reported their MP thin-disk stars are dominant in outer-disk re-

gion. Consequently, what Figure 10 suggests is that the high- $V_\phi$  velocity stars of the MPTN population rotate faster in the outer region. On the other hand, due to their too small  $r_p$  (median  $r_p \sim 4.7 \text{ kpc}$ ) and high eccentricity, the G1 stars reach the solar circle from the inner-disk region.

As far as the SMRTN population is concerned, the lower panels of Figure 10 indicate that there are stars with high eccentricity, low orbital rotation velocity, and small  $r_p$  present. We derived that 52% of the SMRTN stars have  $e < 0.2$ , with a median  $r_p$  of  $7.0 \text{ kpc}$ . The stars with  $e < 0.2$  and  $r_p > 7 \text{ kpc}$  account for 27% of the SMRTN population. A similar trend is reported by Hayden et al. (2018), who showed that a quarter of their metal-rich thin-disk stars have  $r_p > 7 \text{ kpc}$ . On the other hand, Kordopatis et al. (2015) reported that half of super metal-rich thin-disk stars in the Solar vicinity from RAVE DR4 (Kordopatis et al. 2013) have low eccentricity ( $e \leq 0.15$ ).

One step further, we have examined the eccentricity

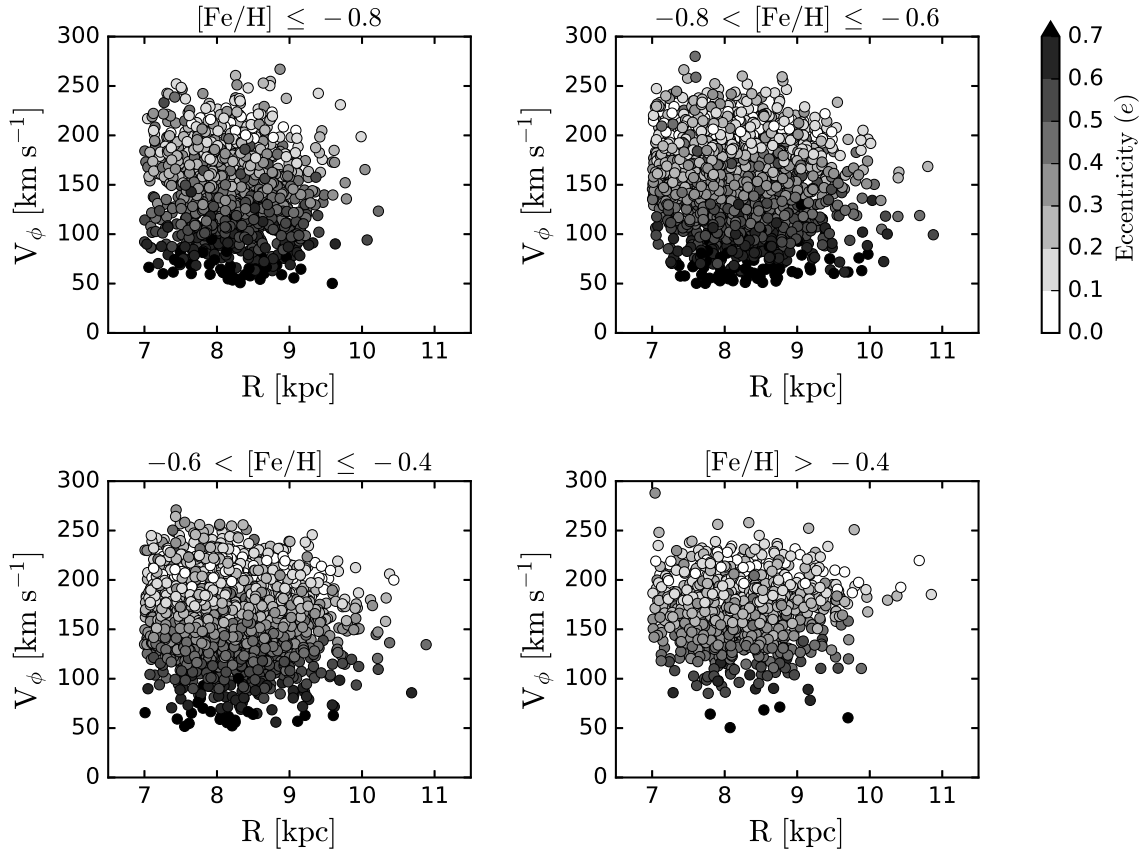


**Figure 11.** Same as in the left panels of Figure 10, but for the thick-disk stars in four metallicity ranges.

distribution in the  $R$ - $V_\phi$  plane for the thick-disk stars, in a similar fashion as for the thin-disk stars shown in the left panels of Figure 10. As can be seen in Figure 11, we have divided the sample into four metallicity bins. Inspection of this figure clearly shows that the fraction of high-eccentricity stars is larger than for the thin-disk population (this is also obvious in Figure 8). Unlike the thin-disk population, however, the high- $e$  ( $> 0.5$ ) stars are mostly concentrated in the region of  $V_\phi < 120$  km s $^{-1}$  for all four metallicity bins. The portion of the high- $e$  stars decreases with increasing metallicity, indicating that the orbits of the more metal-poor thick-disk stars tend to be more perturbed. We found that about 77% of the thick-disk stars have  $r_p < 6$ , with a median value of  $r_p \sim 4.5$  kpc.

#### 4.3. Trends of $Z_{\max}$ and $\sigma_{V_z}$ with $[\alpha/\text{Fe}]$

Finally, we investigated how the  $V_z$  velocity dispersion and maximum vertical distance from the Galactic plane ( $Z_{\max}$ ) change with  $[\alpha/\text{Fe}]$ . Figure 12 displays the trend of  $Z_{\max}$  (top panel) and  $\sigma_{V_z}$  (bottom panel) as a function of  $[\alpha/\text{Fe}]$ , for the thin- (black dots) and thick- (red squares) disk stars. Each symbol represents the median of 500 stars; error bars are calculated from 1000 bootstrap resamples of the 500 stars.

From inspection of the figure, both  $Z_{\max}$  and  $\sigma_{V_z}$  generally rise with increasing  $[\alpha/\text{Fe}]$  for both disk samples. This trend can be understood in the sense that, because the high- $\alpha$  stars are generally old, they have had more time to be perturbed to have higher  $V_z$ , resulting in

larger excursions from the Galactic plane. The high- $\alpha$  thin-disk stars reach as high as  $Z_{\max} = 1.22$  kpc.

This behavior has also been observed by other studies using different stellar samples. For instance, Haywood et al. (2013) obtained high-resolution spectra of F-, G-, and K-type stars, and derived their ages. They separated the thin- and thick-disk populations in the  $[\text{Fe}/\text{H}]$ - $[\alpha/\text{Fe}]$  plane, and found that some of the thin-disk stars are older than 8 Gyrs, which overlaps with the younger thick-disk stars. Note that the age overlap between the thin- and thick-disk stars is also reported by observational and theoretical studies (Delgado Mena et al. 2019; Rojas-Arriagada et al. 2016; Spitoni et al. 2019). However, Spitoni et al. (2019) asserted that the overlap in age might be caused by observational errors, because the uncertainty of asteroseismic ages used in their model tend to increase with increasing age.

Haywood et al. (2013) reported that the oldest metal-poor thin-disk stars have high  $Z_{\max}$ , and that there is a significant increase in  $Z_{\max}$  at near  $[\alpha/\text{Fe}] \sim +0.1$ , which can also be seen in the top panel of Figure 12. Rojas-Arriagada et al. (2016) reported the similar behavior by analyzing the variation of  $|Z|$  distance with  $[\text{Mg}/\text{Fe}]$  for disk-population stars. According to their Figure 7, the  $|Z|$  distance of the MPTN population increases with increasing  $[\text{Mg}/\text{Fe}]$ , and the  $|Z|$  distance of the most  $[\text{Mg}/\text{Fe}]$ -rich stars of the MP thin disk is comparable to that of the youngest (lowest  $[\text{Mg}/\text{Fe}]$ ) thick-disk stars. We also note that there is continuous decrease of  $Z_{\max}$  with declining  $[\alpha/\text{Fe}]$  for the thick-disk stars in the

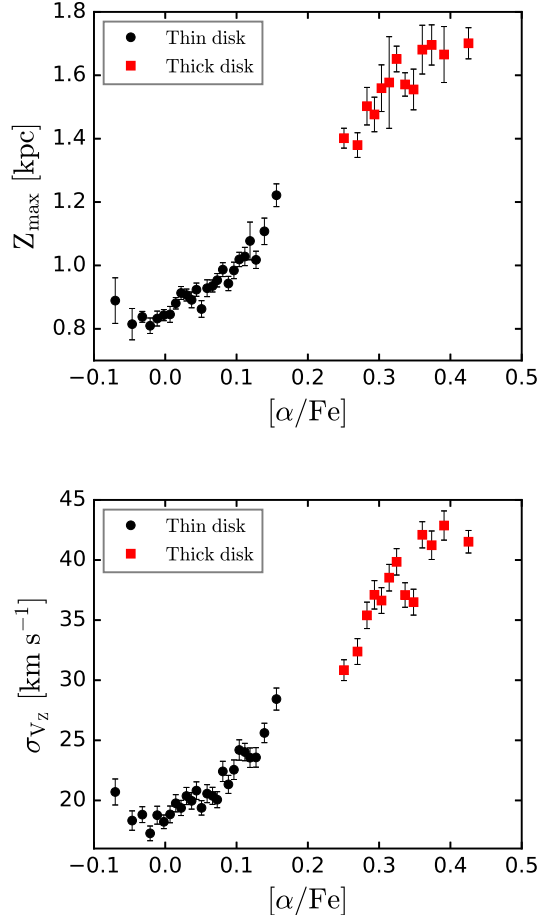


**Figure 12.** Distributions of  $Z_{\max}$  (top panel) and  $\sigma_{V_z}$  (bottom panel), as functions of  $[\alpha/\text{Fe}]$ . Each symbol represents the median of 500 stars; error bars are calculated from 1000 bootstrap resamples of the 500 stars. The black dots and red squares represent the thin- and thick-disk stars, respectively.

top panel of Figure 12. Haywood et al. (2013) and Rojas-Arriagada et al. (2016) found similar trends for the thick disk as well.

In the bottom panel of Figure 12, the highest  $\sigma_{V_z}$  is around  $28 \text{ km s}^{-1}$ , in the most  $\alpha$ -rich bin among the thin-disk population. Haywood et al. (2013) also found an upward trend of  $\sigma_{V_z}$  with increasing  $[\alpha/\text{Fe}]$ ; for the thin-disk sequence, their highest  $\sigma_{V_z} \sim 35 \text{ km s}^{-1}$ , in good agreement with ours. The thick-disk population exhibits a continuous increase of  $\sigma_{V_z}$  with increasing  $[\alpha/\text{Fe}]$ , except for the downward trend shown in the region of  $[\alpha/\text{Fe}] > +0.4$ , which is also reported by Minchev et al. (2014).

## 5. DISCUSSION ON THE DISK FORMATION AND EVOLUTION HISTORY

It is clear from the different dynamical signatures observed in the previous sections that the thin disk and thick disk have experienced different formation and/or evolution histories. Before discussing these formation histories in more detail, we first summarize the main properties of the disk populations we have found:

1. Thin disk – Consists of metal-rich and  $\alpha$ -poor stars. For this population, all three velocity components have negative gradients over  $[\text{Fe}/\text{H}]$ .

Among these, the slope of the  $V_\phi$  component is the steepest ( $\partial V_\phi / \partial [\text{Fe}/\text{H}] = -28.2 \text{ km s}^{-1} \text{ kpc}^{-1}$ ). The gradient of the velocity dispersion is very shallow for all three velocity components. The eccentricity distribution is skewed toward high- $e$  stars. There is a general tendency of the eccentricity to decrease with decreasing  $[\text{Fe}/\text{H}]$  and increasing  $[\alpha/\text{Fe}]$ . Furthermore, there are different kinematic characteristics between the SMRTN and MPTN stars, as addressed below.

(a) SMRTN – Defined by the thin-disk stars with  $[\text{Fe}/\text{H}] > +0.1$ . This population exhibits slower rotation, slightly higher  $e$ , and smaller  $r_p$  with respect to the MPTN stars. Half of the SMRTN stars are found with  $e < 0.2$ . Their median  $r_p$  value is  $\sim 7 \text{ kpc}$ .

(b) MPTN – Consists of thin-disk stars with  $[\text{Fe}/\text{H}] < -0.3$ . This group of stars rotates relatively faster, and exhibits high  $\sigma_{V_z}$  and  $Z_{\max}$ , comparable to the most metal-rich thick-disk stars, particularly for those in the  $\alpha$ -rich region. The stars in the low- $V_\phi$  velocity group (G1) have shorter  $r_p$  than the high- $V_\phi$  velocity stars. The stars with  $V_\phi > 240 \text{ km s}^{-1}$  have relatively high  $e (> 0.2)$ .

2. Thick disk – Comprises chemically metal-poor and  $\alpha$ -rich stars. All three velocity components have positive gradients with  $[\text{Fe}/\text{H}]$ . Among them, the  $V_\phi$  component exhibits the largest gradient ( $\partial V_\phi / \partial [\text{Fe}/\text{H}] = +36.9 \text{ km s}^{-1} \text{ kpc}^{-1}$ ). The dispersions of all three velocity components decline with increasing metallicity. A continuous rise in  $Z_{\max}$  with increasing  $[\alpha/\text{Fe}]$  is found. The eccentricity distribution becomes broader as decreasing  $[\text{Fe}/\text{H}]$  or increasing  $[\alpha/\text{Fe}]$ .

### 5.1. The Super Metal-rich Thin Disk

In Section 4.2, we noted that 27% of our SMRTN stars have low eccentricity and  $r_p > 7 \text{ kpc}$ . This behavior is confirmed by other studies. For example, Kordopatis et al. (2015) reported that even though there are high-eccentricity ( $e > 0.3$ ) stars among their thin-disk stars, most super metal-rich stars have  $e \leq 0.15$  and large orbital radii. Hayden et al. (2018) claimed that the metal-rich stars with  $[\text{Fe}/\text{H}] > +0.1$  and  $r_p > 7 \text{ kpc}$  account for 25% of the stars in their sample, and many stars show low orbital eccentricity. Considering their large  $r_p$ , these stars do not appear to have been formed in a high-metallicity environment such as the inner disk, because they never had the chance to move in the inner-disk region. However, because these stars have low eccentricity, and the metallicity of the interstellar medium (ISM) in the solar neighborhood (SN) is roughly  $[\text{Fe}/\text{H}] = 0$ , as Hayden et al. (2018) claimed, it is plausible to conjecture that these stars in our sample could have been brought from the inner disk into the SN by churning. The more recent study of Hayden et al. (2020) came to the same conclusion, using stars obtained from GALAH. The relatively slow rotation velocity of these stars also support migration from the inner disk by churning.

Theoretically, Minchev et al. (2013) demonstrated that stars born in the region of  $3 < R_0$  (birth radius)  $< 5$

kpc can contribute to an increase in the metallicity in the SN by up to 0.6 dex through radial migration, while stars that are born locally end up with  $[\text{Fe}/\text{H}] \sim 0.15$ , implying that the SMRTN stars were born in the inner disk rather than the SN.

The above claim is supported by the trend of the velocity dispersion over  $[\text{Fe}/\text{H}]$  for the SMRTN stars as shown in Figure 7. The figure indicates that the gradient of  $\sigma_{V_z}$  is slightly negative, while a small positive gradient for  $\sigma_{V_\phi}$ . The lower  $\sigma_{V_z}$  at the solar metallicity can be explained by the bias that the stars close to the Galactic mid-plane have more tendency to migrate because they have relatively lower vertical velocity dispersion than the ones further away from the Galactic mid-plane. Consequently, the migrated stars do not show high velocity dispersion, but rather cooler dispersion (Vera-Ciro et al. 2014, 2016). The positive gradient of  $\sigma_{V_\phi}$  can be explained by the spread of the changed angular momenta of the migrated star.

How can we interpret the stars with high eccentricity and small perigalacticon distances ( $r_p < 5$  kpc) among the SMRTN stars? These stars account for about 22% of the SMRTN population. The broader observed  $e$ -distribution for the low  $\alpha$ -stars in Figure 8 is due to the presence of these stars. As a result of their shorter perigalacticon distances, these stars are mostly found at the apogalacticons of their orbits, due to their slower (low- $V_\phi$  velocities) orbital motions there. Therefore, it is plausible to explain that the SMRTN stars with high eccentricity came from the inner disk by blurring. This interpretation is upheld by studies of Pompéia et al. (2002) and Trevisan et al. (2011), who also claimed that metal-rich stars on non-circular orbits have come from the inner disk.

### 5.2. The Metal-Poor Thin Disk

Provided that there exists a general increasing trend of stellar age with increasing  $[\alpha/\text{Fe}]$ , as most recent studies suggest (Delgado Mena et al. 2019; Nissen et al. 2017; Silva Aguirre et al. 2018), we can suppose that the MPTN stars are older than the SMRTN stars because of their higher  $[\alpha/\text{Fe}]$ , in spite of their undetermined ages. This group of stars in our sample also has mostly high orbital velocity ( $V_\phi > 180$  km s $^{-1}$ ), low-eccentricity ( $e < 0.3$ ), and large  $r_p$  ( $> 7$  kpc), as seen in Figure 10. One notable feature in this group of stars is the existence of stars with high  $V_\phi$  ( $> 240$  km s $^{-1}$ ) and  $e > 0.2$ . Furthermore, Figure 12 indicates that the MPTN stars show slightly lower  $Z_{\text{max}}$  and  $\sigma_{V_z}$  than those of the  $[\alpha/\text{Fe}]$ -poor thick-disk stars.

One possible interpretation on the origin of the high- $V_\phi$  stars among the ones with  $e > 0.2$  is the radial movement by churning from the outer disk, as these stars have high- $V_\phi$ , large  $r_p$ , and lower metallicity than the ISM in the SN. In this regard, Haywood et al. (2013) proposed that the oldest thin-disk stars appear to be of outer-disk origin, as they rotate rapidly with nearly circular orbits. According to their study, there is a barrier between the inner and outer disks due to outer Lindblad resonance (Lynden-Bell & Kalnajs 1972), resulting in the isolated and disconnected evolution of the outer disk from the inner disk. Unless some of the high- $V_\phi$ , MPTN stars have moved from the outer disk as proposed by Haywood et al., we would not observe those stars in the SN today.

The higher  $V_z$  dispersion of the MPTN stars compared with the SMRTN stars also supports the radial migration hypothesis, as the inward migrators tend to increase the  $V_z$  dispersion of such stars at their final destination (Vera-Ciro et al. 2014). The negative slope of the  $V_\phi$  component over  $[\text{Fe}/\text{H}]$  also provides another clue to the radial migration, because the stars that arrive from the outer disk should have higher angular momentum than the ones in the final location of the migrated stars.

However, the G1 stars ( $[\text{Fe}/\text{H}] < -0.3$  and low- $V_\phi$ ), required another mechanism to explain their high eccentricities. Owing to their small  $r_p$ , they are mostly observed at apogalacticon. Thus, we can infer from the low metallicity, high- $[\alpha/\text{Fe}]$ , and relatively low- $V_\phi$  of these stars that they formed early in the inner disk when the ISM was not yet enriched with heavy elements, and moved outward due to blurring to reach the Solar circle.

As Rojas-Arriagada et al. (2016) suggested, this population might experience independent chemodynamical evolution, distant from that of their metal-rich counterparts. They reported that the smooth change of  $|Z|$  with  $[\text{Fe}/\text{H}]$  implies that the dynamical evolution occurred quietly without much violent events such as a merger. However, the steep increase of  $Z_{\text{max}}$  and  $\sigma_{V_z}$  with  $[\alpha/\text{Fe}]$  may suggest a different evolution, as the G1 stars may have been influenced by dynamical heating by a minor merger. *Gaia*-Enceladus (Helmi et al. 2018) or the Splashed Disk (Belokurov et al. 2020) may be good examples of such mergers.

To summarize, our results suggest that the high-metallicity thin-disk stars moved from the inner disk, while the low-metallicity thin-disk stars migrated from the outer disk, or from the inner disk, through more churning than blurring. In line with this interpretation, using red giant stars from APOGEE DR14 (and *Gaia* parallaxes), Feltzing et al. (2020) attempted to quantify the degree of radial migration by blurring and churning. They found that about 10–50% of their sample experienced churning or blurring over the metallicity range from  $[\text{Fe}/\text{H}] \sim -0.7$  to  $\sim +0.3$ , even though the fraction varies depending on the constraints imposed from the circularity of their orbits. In addition, a recent study by Frankel et al. (2020) also demonstrated that the evolution of the  $\alpha$ -poor thin-disk stars is more influenced by churning, which agrees with our interpretation. From this line of reasoning, we can conclude that radial mixing by churning and blurring may have had a more dominant influence in shaping the current thin-disk structure of the MW, compared with other suggested mechanisms such as accretion and/or disk-heating by mergers.

### 5.3. The Thick Disk

There is clear kinematic distinction between the thin and thick disks – the continuous decrease of  $\sigma_{V_R}$ ,  $\sigma_{V_\phi}$ , and  $\sigma_{V_z}$  with increasing  $[\text{Fe}/\text{H}]$  for the thick disk, but an almost flat gradient over metallicity for the thin disk, as shown in Figure 7. The most notable kinematic difference between the two populations is the gradient of the rotation velocity over  $[\text{Fe}/\text{H}]$ . We found  $\partial V_\phi / \partial [\text{Fe}/\text{H}] = -28.2$  km s $^{-1}$  dex $^{-1}$  and  $+36.9$  km s $^{-1}$  dex $^{-1}$  for the thin and thick disk, respectively. The trend of higher eccentricity with decreasing metallicity is also characteristic of the thick-disk population. These are tell-tale signs of

the different formation histories between the two disks. Below, we attempt to associate our findings with the proposed formation models of the thick disk.

The positive gradient of the rotation velocity is mostly reproduced by various radial migration models. For instance, [Loebman et al. \(2011\)](#) carried out a simulation of radial migration and identified  $\partial V_\phi / \partial [\text{Fe}/\text{H}] \sim -24.8 \text{ km s}^{-1} \text{ dex}^{-1}$  for their low- $[\alpha/\text{Fe}]$  stars, while a mild positive gradient ( $\sim +13.5 \text{ km s}^{-1} \text{ dex}^{-1}$ ) was obtained for their high- $[\alpha/\text{Fe}]$  stars, although this gradient is substantially smaller than observed for the thick-disk population. [Curir et al. \(2012\)](#) investigated the evolution of the thick disk by simulated collisionless particles, and found a positive gradient of  $+60 \text{ km s}^{-1} \text{ dex}^{-1}$  for the thick disk, which is comparable with the observational result. Recent studies ([Kawata et al. 2017](#); [Schönrich & McMillan 2017](#)) also demonstrated that the inside-out and upside-down formation of the thick disk, along with radial migration, can readily reproduce the observed positive slope of orbital rotation velocity with  $[\text{Fe}/\text{H}]$ .

Moreover, as shown in [Figure 8](#), we observe that the eccentricity distribution of the thick disk varies according to  $[\alpha/\text{Fe}]$  and  $[\text{Fe}/\text{H}]$ , and the number of stars with high eccentricity is reduced with decreasing  $[\alpha/\text{Fe}]$  or increasing  $[\text{Fe}/\text{H}]$ . This behavior is reproducible by the radial migration model ([Sales et al. 2009](#)), which produces relatively small numbers of high-eccentricity stars for the thick-disk component, consistent with the shape of the  $e$ -distribution of our sample. These results point to a radial migration as an important part of the thick-disk formation history. Nonetheless, [Minchev et al. \(2012\)](#) suggested that the impact of radial migration on the thickening the disk is not significant.

In [Figure 6](#), we noted that the velocity dispersions ( $\sigma_{V_R}$ ,  $\sigma_{V_\phi}$ , and  $\sigma_{V_z}$ ) decline continuously with increasing  $[\text{Fe}/\text{H}]$ . In addition, the top panel of [Figure 12](#) indicates that  $Z_{\text{max}}$  continuously declines with decreasing  $[\alpha/\text{Fe}]$ . From these characteristics, it is challenging to imagine that the thick-disk stars were accreted, as they would be expected to have similar velocity dispersions. Rather, we can infer that the star-forming environment could have stabilized with decreasing  $[\alpha/\text{Fe}]$  during the thick-disk formation phase, if we use  $[\alpha/\text{Fe}]$  as a proxy for a stellar age in the thick disk. A tight correlation has been reported between  $[\alpha/\text{Fe}]$  and age for the thick-disk population ([Haywood et al. 2013](#); [Bensby et al. 2014](#)). However, caution may need to be taken, since the recent study by [Silva Aguirre et al. \(2018\)](#) found no correlation between age and  $[\alpha/\text{Fe}]$  for the thick-disk population, based on a sample of red giants with asteroseismic ages. These authors also reported that the velocity dispersion is not well-correlated with age for the high- $\alpha$  stars. One pitfall of this study is that the uncertainty of their asteroseismic age is rather large. The median uncertainty is about 28.5%, and becomes larger with increasing age. In their independent study, [Spitoni et al. \(2019\)](#) claimed that the overlapping ages between the thin- and thick-disk stars arose from uncertainties in the asteroseismic ages. Thus, the existence of any correlations between age and  $[\alpha/\text{Fe}]$  must be confirmed in the future with better-constrained age determinations.

Nevertheless, the observed kinematic features can be seen in the gas-rich merger models. According to [Brook](#)

[et al. \(2004, 2007, 2012\)](#)), the thick disk can be formed from accreted gas during a chaotic merger period. This model also predicts that cooler kinematics (e.g., low velocity dispersions) appear to emerge for the younger disk stars formed by gas-rich mergers at later times;  $\sigma_{V_z}$  of stars formed at  $z = 1.0$  are smaller than the velocity dispersions of stars formed at  $z = 1.5$ . The epochs at  $z = 1.0$  and  $z = 1.5$  are the dominant phases of thick-disk formation in the simulation by [Brook et al. \(2012\)](#). These can be interpreted such that the thick disk becomes stabilized with decreasing age, which qualitatively agrees with the bottom panel of [Figure 12](#), if we consider  $[\alpha/\text{Fe}]$  to be a stellar-age proxy. Furthermore, the thick-disk stars in our sample tend to have various eccentricities, from low to high, for all metallicity bins, as shown in [Figure 11](#). In particular, the diversity of the eccentricity distributions with a wide range of the  $V_\phi$  velocity for the most metal-poor bin (top-left panel of [Figure 11](#)) probably indicates a hot and violent state when they were born, or at least the kinematic evolution of those stars. One downside of this mechanism is, however, the difficulty of reconciling the very high- $e$  stars produced by the model with the absence of such high- $e$  stars in the observed data. [Sales et al. \(2009\)](#) suggested that the gas-rich merger scenario can make stars on non-circular orbits that extend to  $e \sim 0.8$ .

Nonetheless, the cosmological hydrodynamical simulations performed by [Buck \(2020\)](#) support the gas-rich merger model as a thick-disk formation model, demonstrating that the low- and high- $\alpha$  sequences observed in the Galactic disk naturally arise through a gas-rich merger. In the simulations, the high- $\alpha$  stars formed first, and the low- $\alpha$  stars formed after fresh metal-poor gas was injected into the disk by the merging satellite. These simulations also showed that the disk stars were greatly influenced by secular evolution, such as migration, that is, the low- $\alpha$  stars came from both the inner and outer disk, whereas the high- $\alpha$  stars mostly migrated from the inner disk, which qualitatively agrees with our interpretation.

In line with the gas-rich merger models, it is worth mentioning that a thick disk formed from turbulent clumps can have stars on highly eccentric orbits, as gravitational instabilities make stars and gas disperse during the clumpy phase (e.g., [Bournaud et al. 2009](#); [Robin et al. 2014](#); [Bournaud et al. 2014](#); [Elmegreen et al. 2017](#)). The notable feature of this scenario is the decreasing scale height of the thick disk over time, which is qualitatively in good agreement with the observations (see [Figure 12](#)).

There is, however an assertion that the metal-poor and  $[\alpha/\text{Fe}]$ -rich stars exhibit relatively constant kinematic trend (e.g., [Minchev et al. 2014](#)). This constant but high velocity dispersion can be observed in our sample (bottom panel of [Figure 12](#)); there exists a plateau (or only slightly downward trend) of  $\sigma_{V_z}$  for the  $[\alpha/\text{Fe}]$  rich bins. To confirm this further, we divided our sample into several metallicity bins, and then, checked the velocity dispersion as a function of  $[\alpha/\text{Fe}]$  again. In this exercise, we obtained a decreasing velocity dispersion in the range of  $-1.2 < [\text{Fe}/\text{H}] < -0.9$ . This behavior can be seen at the lowest  $[\text{Fe}/\text{H}]$  bin in [Figure 7](#). [Minchev et al. \(2014\)](#) proposed that the decreasing velocity dispersion over  $[\alpha/\text{Fe}]$  arises from radial migration, triggered by a merger with a mass ratio of 1 to 5 about 8 – 9

Gyrs ago. They emphasized that an external event such as a significant merger is necessary to trigger the radial migration rather than just the operation of an internal, secular process.

Recent studies also indicate that the dynamical heating of the disk by mergers contributes to the formation of the thick disk. For example, [Belokurov et al. \(2020\)](#) used the *Gaia* DR2 and various spectroscopic data to identify a large number of metal-rich ( $[\text{Fe}/\text{H}] > -0.7$ ) stars on highly eccentric orbits. They claimed that this population, referred to as the ‘‘Splashed Disk’’, is linked to the  $\alpha$ -rich thick disk, and has halo-like kinematics. They argued that the Splashed-Disk stars were born in the proto-disk of the MW, and their orbits were changed by a massive ancient accretion event such as *Gaia*-Enceladus. However, their Splashed-Disk stars have much lower rotation velocities than our thick-disk population. [An & Beers \(2020\)](#) confirmed these properties, that the Splashed-Disk stars show similar metallicity to the canonical thick disk, but their kinematics differ. [Helmi et al. \(2018\)](#) also showed, from *Gaia* DR2 and APOGEE DR14 data, that a dwarf satellite whose debris contributes significantly to the inner-halo population, caused the dynamical heating of a pre-existing disk to form the thick disk.

To sum up, the kinematic and chemical characteristics observed for our thick-disk stars suggest that the thick disk is formed by a turbulent gas-rich merger in an inside-out fashion, as the cosmological simulations by [Schönrich & McMillan \(2017\)](#) and [Kawata et al. \(2017\)](#) demonstrated. During the mergers and later evolution, the dynamical heating of the pre-existing disk and stellar radial migration have influenced the evolution of the thick disk further. This interpretation partly agrees with the results from recent cosmological simulations by [Grand et al. \(2020\)](#). They showed that the progenitor of *Gaia*-Enceladus and the *Gaia*-Sausage induced gas-rich mergers to form the high  $\alpha$ -thick disk stars, and heated the proto-Galactic disk to generate the positive correlation between  $V_\phi$  and  $[\text{Fe}/\text{H}]$ . Consequently, it appears that various physical mechanisms have played roles in structuring the current thick disk; a single formation scenario or mechanism is not able to explain all the observed properties.

## 6. SUMMARY

We have made use of SEGUE G- and K-type dwarfs to investigate the chemodynamical properties of the Galactic disk system, after separation into an  $\alpha$ -poor thin and an  $\alpha$ -rich thick disk. The dynamical properties of the thin-disk stars indicate that some fraction of the MPTN stars radially move from the outer disk or the inner disk, while some fraction of the SMRTN stars may originate from the inner disk. Radial migration is required to explain these phenomena. Churning, in particular, may have greatly influenced to create the current structure of the thin disk, while we cannot neglect the importance of the blurring for the high-eccentricity stars.

According to our results, the formation of the thick disk can be explained by violent mechanisms, such as gas-rich mergers or giant turbulent clumps, as these models can readily produce significant numbers of high-eccentricity stars, as well as the thinner and more stable thick disk with decreasing  $[\alpha/\text{Fe}]$  (or increasing  $[\text{Fe}/\text{H}]$ ).

During the merger, and the later evolution, the dynamical heating of a pre-existing disk, as well as radial migration, may both play roles in forming the current thick disk.

We thank an anonymous referee for his/her careful review of this paper to improve the clarity of the presentation.

Funding for SDSS-III has been provided by the Alfred P. Sloan Foundation, the Participating Institutions, the National Science Foundation, and the U.S. Department of Energy Office of Science. The SDSS-III Web site is <http://www.sdss3.org/>.

Y.S.L. acknowledges support from the National Research Foundation (NRF) of Korea grant funded by the Ministry of Science and ICT (No.2017R1A5A1070354 and NRF-2018R1A2B6003961). T.C.B. acknowledges partial support for this work from the grant PHY 14-30152; Physics Frontier Center/JINA Center for the Evolution of the Elements (JINA-CEE), awarded by the US National Science Foundation.

## REFERENCES

- Abadi, M. G., Navarro, J. F., Steinmetz, M., & Eke, V. R. 2003, *ApJ*, 597, 21
- Abolfathi, B., et al. 2018, *ApJS*, 235, 42
- Adibekyan, V. Z., Santos, N. C., Sousa, S. G., & Israelian, G. 2011, *A&A*, 525, L11
- Adibekyan, V. Z., Figueira, P., Santos, N. C., et al. 2013, *A&A*, 554, A44
- Allende Prieto, C., Sivarani, T., Beers, T. C., et al. 2008, *AJ*, 136, 2070
- Anders, G., et al. 2014, *A&A*, 564, A115
- An, D., & Beers, T. C. 2020, *ApJ*, submitted
- Bailer-Jones, C. A. L., Rybizki, J., Foesneau, M., Mantelet, G., & Andrae, R. 2018, *AJ*, 156, 58
- Belokurov, V., Erkal, D., Evans, N. W., Koposov, S. E., & Deason, A. J. 2018, *MNRAS*, 478, 611
- Belokurov, V., Sanders, J. L., Fattahi, A., et al. 2020, *MNRAS*, in press, [arXiv:1909.04679](https://arxiv.org/abs/1909.04679)
- Bensby, T., Feltzing, S., & Lundström, I. 2003, *A&A*, 410, A527
- Bensby, T., Feltzing, S., & Oey, M. S. 2014, *A&A*, 562, A71
- Bland-Hawthorn, J., & Gerhard, O. 2016, *ARA&A*, 54, 529
- Boeche, C., Siebert, A., Piffl, T., et al. 2013, *A&A*, 559, A59
- Bovy, J., Rix, H.-W., Hogg, D. W., et al. 2012b, *ApJ*, 755, 115
- Bovy, J., Rix, H.-W., & Hogg, D. W. 2012a, *ApJ*, 751, 131
- Bovy, J. 2015, *AJ*, 216, 29
- Brook, C. B., Kawata, D., Gibson, B. K., & Freeman, K. C. 2004, *ApJ*, 612, 894
- Brook, C., Richard, S., Kawata, D., Martel, H., & Gibson, B. K. 2007, *ApJ*, 658, 60
- Brook, C. B., Stinson, G. S., Gibson, B. K., et al. 2012, *MNRAS*, 426, 690
- Bournaud, F., Elmegreen, B. G., & Martig, M. 2009, *ApJ*, 707, L1
- Bournaud, F., Perret, V., Renaud, F., et al. 2014, *ApJ*, 780, 57
- Buck, T. 2020, *MNRAS*, 491, 5435
- Casetti-Dinescu, D. I., Girard, T. M., Korchagin, V. I., & van Altena, W. F. 2011, *ApJ*, 728, 7
- Chen, B. B., Liu, X. W., Yuan, H. B., et al. 2018, *MNRAS*, 476, 3278
- Carollo, D., Chiba, M., Ishigaki, M., et al. 2019, *ApJ*, 887, 22
- Curir, A., Lattanzi, M. G., Spagna, A., et al. 2012, *A&A*, 545, A133
- Delgado Mena, E., Moya, A., Adibekyan, V., et al. 2019, *A&A*, 624, 78
- De Silva, G. M., et al. 2015, *MNRAS*, 449, 2604
- Dierickx, M., Klement, R. J., Rix, H.-W., & Liu, C. 2010, *ApJ*, 725, L186
- Elmegreen, B. G., Elmegreen, D. M., Tompkins, B., & Jenks, L. G. 2017, *ApJ*, 847, 14



- Gaia Collaboration, Brown, A. G. A., Vallenari, A., et al. 2018, *A&A*, 616, 1
- Gilmore, G., & Reid, N. 1983, *MNRAS*, 202, 1025
- Gilmore, G., Randich, S., Asplund, M., et al. 2012, *The Messenger*, 147, 25
- Grand, R. J. J., Kawata, D., Belokurov, V., et al. 2020, *MNRAS*, [arXiv:2001.06009](https://arxiv.org/abs/2001.06009)
- Guiglion, G., Recio-Blanco, A., de Laverny, P., et al. 2015, *A&A*, 583, A91
- Feltzing, S., Bowers, B. B., & Agertz, O. 2020, *MNRAS*, 493, 1419
- Frankel, N., Snaders, J., Ting, Y.-S., & Rix, H.-W. 2020, *ApJ*, submitted, [arXiv:2002.04622](https://arxiv.org/abs/2002.04622)
- Fuhrmann, K. 1998, *A&A*, 338, 161
- Fuhrmann, K. 2008, *MNRAS*, 384, 173
- Hayden, M. R., Bovy, J., Holtzman, J. A., et al. 2015, *ApJ*, 808, 132
- Hayden, M. R., Recio-Blanco, A., de Laverny, P., et al. 2018, *A&A*, 609, A79
- Hayden, M. R., Bland-Hawthorn, J., Sharma, S., et al. 2020, *MNRAS*, 493, 2952
- Haywood, M., Di Matteo, P., Lehnert, M. D., Katz, D., & Gómez, A. 2013, *A&A*, 560, A109
- Helmi, A., Babusiaux, C., Koppelman, H., et al. 2018, *Nature*, 563, 85
- Hogg, D. W., Blanton, M. R., Roweis, S. T., & Johnston, K. V. 2005, *ApJ*, 629, 268
- Jing, Y., Du, C., Gu, J., et al. 2016, *MNRAS*, 463, 3390
- Jurić, M., Ivezić, Ž., Brooks, A., et al. 2008, *ApJ*, 673, 864-914
- Kawata, D., Grand, R. J. J., Gibson, B. K., et al. 2017, *MNRAS*, 464, 702
- Kerr, F. J., & Lynden-Bell, D. 1986, *MNRAS*, 221, 1023
- Kordopatis, G., Recio-Blanco, A., de Laverny, P., et al. 2011, *A&A*, 535, 107
- Kordopatis, G., Gilmore, G., Steinmetz, M., et al. 2013, *AJ*, 146, 134
- Kordopatis, G., Binney, J., Gilmore, G., et al. 2015, *MNRAS*, 447, 3526
- Lee, Y. S., Beers, T. C., Sivarani, T., et al. 2008a, *AJ*, 136, 2022
- Lee, Y. S., Beers, T. C., Sivarani, T., et al. 2008b, *AJ*, 136, 2050
- Lee, Y. S., Beers, T. C., Allende Prieto, C., et al. 2011a, *AJ*, 141, 90
- Lee, Y. S., Beers, T. C., An, D., et al. 2011b, *ApJ*, 738, 187
- Li, C., & Zhao, G. 2017, *ApJ*, 850, 25
- Lindgren, L., Hernández, J., Bombrun, A., et al. 2018, *A&A*, 616, 2
- Lo Curto, G., Mayor, M., Benz, W., et al. 2010, *A&A*, 512, A48
- Loebman, S. R., Roškar, R., Debattista, V. P., et al. 2011, *ApJ*, 737, 8
- Luo, A.-L., Zhao, Y.-H., Zhao, G., et al. 2015, *RAA*, 15, 1095
- Lutz, T. E. & Kelker, D. H. 1973, *PASP*, 85, 573
- Lynden-Bell, D., & Kalnajs, A. J. 1972, *MNRAS*, 157, 1
- Majewski, S. R., Schiavon, R. P., Frinchaboy, P. M., et al. 2017, *AJ*, 154, 94
- Mayor, M., Pepe, F., Queloz, D., et al. 2003, *The Messenger*, 114, 20
- Mikolaitis, Š., Hill, V., Recio-Blanco, A., et al. 2014, *A&A*, 572, A33
- Minchev, I., Famaey, B., Quillen, A. C., & Dehnen, W. 2012, *European Physical Journal Web of Conferences*, 19, 07002
- Minchev, I., Chiappini, C., & Martig, M. 2013, *A&A*, 558, A9
- Minchev, I., Chiappini, C., Martig, M., et al. 2014, *ApJ*, 781, L20
- Mints, A., & Hekker, S. 2019, *A&A*, 621, 17
- Nandakumar, G., Schultheis, M., Hayden, M., et al. 2017, *A&A*, 606, 97
- Nissen, P. E., Silva Aguirre, V., Christensen-Dalsgaard, J., Collet, R., Grundahl, F., & Slumstrup, D. 2017, *A&A*, 608, 112
- Pompéia, L., Barbuy, B., & Grenon, M. 2002, *ApJ*, 566, 845
- Recio-Blanco, A., de Laverny, P., Kordopatis, G., et al. 2014, *A&A*, 567, A5
- Reddy, B. E., Lambert, D. L., & Allende Prieto, C. 2006, *MNRAS*, 367, 1329
- Roškar, R., Debattista, V. P., Quinn, T. R., Wadsley, J. 2012, *MNRAS*, 426, 2089
- Robin, A. C., Reylé, C., Fliri, J., et al. 2014, *A&A*, 569, A13
- Re Fiorentin, P., Lattanzi, M. G., & Spagna, A. 2019, *MNRAS*, 484, L69
- Rojas-Arriagada, A., Recio-Blanco, A., de Laverny, P., et al. 2016, *A&A*, 586, A39
- Sales, L. V., Helmi, A., Abadi, M. G., et al. 2009, *MNRAS*, 400, L61
- Sellwood, J. A., & Binney, J. J. 2002, *MNRAS*, 336, 785
- Santos, N. C., Mayor, M., Bonfils, X., et al. 2011, *A&A*, 526, A112
- Schlesinger, K. J., Johnson, J. A., Rockosi, C. M., et al. 2012, *ApJ*, 761, 160
- Schönrich, R., & Binney, J. 2009, *MNRAS*, 396, 203
- Schönrich, R., & McMillan, P. J. 2017, *MNRAS*, 467, 1154
- Silva Aguirre, V., Bojsen-Hansen, M., Slumstrup, D., et al. 2018, *MNRAS*, 475, 5487
- Smolinski, J. P., Lee, Y. S., Beers, T. C., et al. 2011, *AJ*, 141, 89
- Soubiran, C., Bienaymé, O., & Siebert, A. 2003, *A&A*, 398, 141
- Spitoni, E., Silva Aguirre, V., Matteucci, F., Calura, F., & Grisoni, V. 2019, *A&A*, 623, 60
- Steinmetz, M., Zwitter, T., Siebert, A., et al. 2006, *AJ*, 132, 1645
- Trevisan, M., Barbuy, B., Eriksson, K., et al. 2011, *A&A*, 535, A42
- Vera-Ciro, C., D’Onghia, E., Navarro, J., & Abadi, M. 2014, *ApJ*, 794, 173
- Vera-Ciro, C., D’Onghia, E., & Navarro, J. 2016, *ApJ*, 833, 42
- Villalobos, Á., & Helmi, A. 2008, *MNRAS*, 391, 1806
- Wilson, M., et al. 2011, *MNRAS*, 413, 2235
- Wojno, J., Kordopatis, G., Steinmetz, M., et al. 2016, *MNRAS*, 461, 4246
- Wojno, J., Kordopatis, G., Piffl, T., et al. 2017, *MNRAS*, 468, 3368
- Wyse, R. F. G., & Gilmore, G. 1995, *AJ*, 110, 2771
- Yan Y., Du, C., Liu, S. et al. 2019, *ApJ*, 880, 36
- Yanny, B., Rockosi, C., Newberg, H. J., et al. 2009, *AJ*, 137, 4377
- York, D. G., et al. 2000, *AJ*, 120, 1579
- Yoshii, Y. 1982, *PASJ*, 34, 365